Politecnico di Torino

université PARIS-SACLAY

Université de Paris

Self-organization of Active Mixtures

Candidate: Alberto Dinelli

Supervisors: Julien Tailleur,
Alessandro Pelizzola,
Martin Lenz

International track of Physics of Complex Systems

July 2021

Table of Contents

Abstract

Self-organization is ubiquitous in biological systems at all scales, from the animal world down to the intra-cellular environment. In all these systems, the dynamics of micro-constituents can lead to emergent large-scale behaviours, such as static patterns or collective motion. Active matter provides a solid framework to explain the physics behind these processes at many different scales.
So far, the literature on the subject has mostly focused on single-component active systems; nonetheless, monodispersity imposes strong limitations on the complexity of the emergent macroscopic phases. In order to obtain less idealised self-assembling structures like the ones encountered in biology, heterogeneity must be included.
In this work we study the macroscopic phenomenology of N-component active mixtures of run-and-tumble particles (RTPs) interacting via quorum-sensing (QS), with both numerical and analytical tools. Microscopic simulations are employed to study the macroscopic phases of binary active mixtures, with a special focus on dynamic patterns. To explain the emergence of the observed phases, we coarse-grain the microscopic theory to derive the macroscopic dynamics of the density fields. Via mean-field approximation and linear stability analysis of the field theory, we relate the microscopic parameters to the emergent large-scale patterns.
Finally, we study under which conditions on the microscopic dynamics an active mixture of RTPs exhibits time-reversal symmetry (TRS) at the macroscopic level. When this occurs, the active mixture is macroscopically equivalent to an equilibrium passive system. In particular, we show that such a mapping to equilibrium can exist only if microscopic QS-interactions between different strains are reciprocal.

Keywords: active matter, run-and-tumble particles, bacteria, non-equilibrium systems, phase transitions, mixture, self-organization, pattern formation, Cahn-Hilliard

Acknowledgements

A mamma e babbo, che mi sono sempre stati accanto durante questo percorso. Anche nei mesi più difficili della pandemia, siete riusciti a supportarmi in ogni momento. Vi sarò per sempre grato di tutte le opportunità che mi avete regalato nella vita. Spero di riuscire a rendervi orgogliosi.

Agli zii Andrea e Irina, che mi hanno sempre accolto con affetto e calore durante i viaggi tra casa e Parigi.

A Luca, Fra e Costa, insostituibili compagni di avventura in questi due anni di laurea magistrale. Insieme abbiamo condiviso tanto: quotidianità, esami, progetti e sogni per il futuro. Spero che le nostre strade possano sempre continuare ad incrociarsi.

A Julien, che mi ha pazientemente seguito durante questi mesi di tirocinio, aiutandomi a muovere i primi passi nel mondo della ricerca ed offrendomi continue opportunità di crescita.

A tutti i miei amici di una vita: Paolo, Lore, Ale, Fili, Gabri, Jack, Ali, Giulia, Sara, Ele, e a tutti quelli che non riesco a nominare qua. Grazie per aver addolcito la distanza in questa prima esperienza lontano da casa.

A Leo e Laura, sempre presenti al mio fianco, che sia in videochiamata o sui sentieri del Gran Paradiso. Grazie per aver sostenuto ogni mio passo con tanto entusiasmo ed affetto.

A tutti i Cavalieri del Chioschetto, che hanno reso indimenticabili i tre anni a Pisa, e che tuttora sono la mia grande famiglia di fisici (e non solo).

A tutti i colleghi del laboratorio MSC, che mi hanno fatto sentire accolto sin dal primo giorno, e con cui spero di coltivare un solido rapporto in futuro.

Ai professori Pelizzola e Lenz, per i loro contributi a questa tesi e per aver acceso in me, per primi, un vivo interesse nelle applicazioni biologiche della fisica statistica.

A tutti gli organizzatori e professori del master PCS, per aver reso l'esperienza di questi anni tanto formativa, nonostante le enormi difficoltà dovute alla pandemia.

A Mattia, Fili, Ali, Save, e tutte le splendide persone che ho incontrato in questo percorso e che, giorno dopo giorno, hanno arricchito questi due anni di vita.

Grazie a tutti!

Alberto Dinelli

Chapter 1

Introduction

1.1 What is active matter?

Active matter defines systems whose fundamental constituents convert internal energy into self-propulsion forces, driving the system out of equilibrium at microscopic level. Active particles are found at all scales in biology, from the animal world (e.g. bird flocks, schools of fish) down to the cellular scale (e.g. epitelial cells, bacterial colonies) or even below (e.g. acto-myosin networks in the cytoskeleton). In all these examples, the micro-constituents are capable of *self-organizing* into complex structures, exhibiting *collective motion* at the macroscopic scale (Figure 1.1).

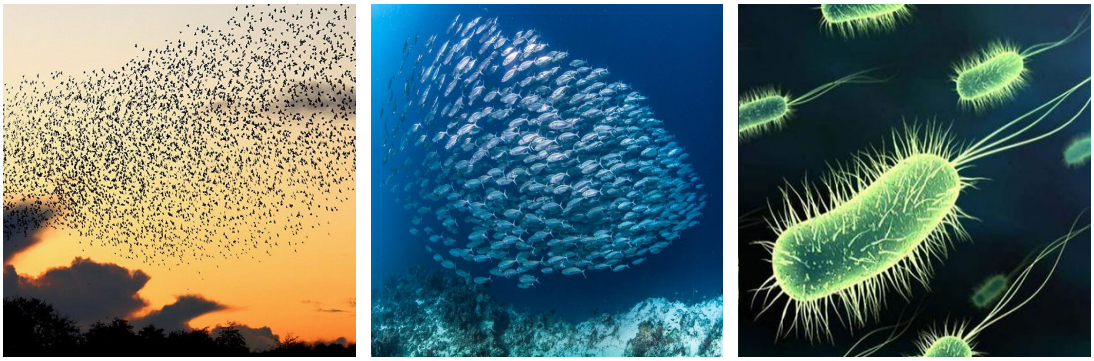

Figure 1.1: Biological examples of active systems: from flocks of starlings, to schools of sardines and bacterial colonies.

In addition to this, in the last two decades experimentalists have engineered *synthetic active systems*, paving the way towards self-assembling materials. Such systems are typically made up of micrometric beads that can be activated by chemical pro-

cesses, electric fields, or even by light (Figure 1.2). From clustering in the absence of adhesive forces [1] to traveling waves [2], to dynamic lane formation and breaking [3], the phenomenology of these systems has no counterpart in passive colloids (Figure 1.3).

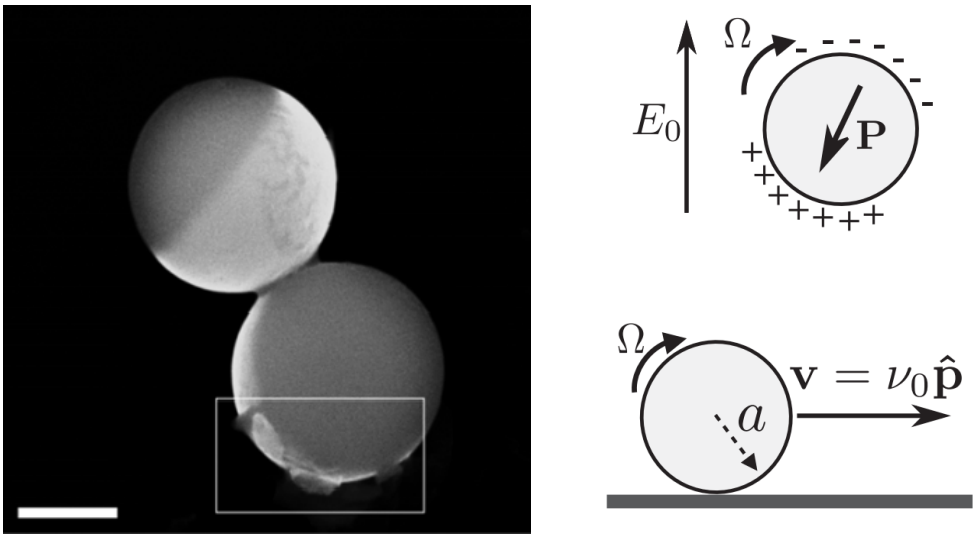

Figure 1.2: *Left*: Janus colloids are micrometric silica beads that are half-coated, e.g. in platinum. When immersed in a hydrogen peroxide substrate, the Pt-coated side reacts with it, causing the particle to self-propel [4]). *Right*: Quincke rollers consist in insulating spheres that are immersed in a conducting fluid, e.g. a saline solution. When the system is subjected to an external electric field, the beads polarize and an electrostatic torque is generated, leading to the rolling motion of the bead [5].

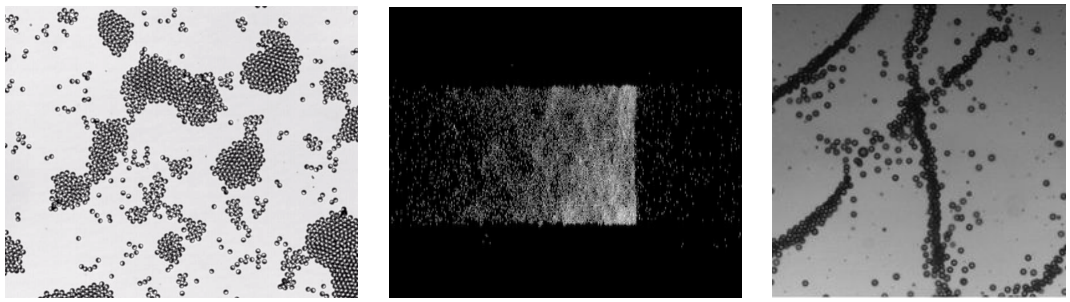

Figure 1.3: *Left*: Motility-induced clustering of Janus colloids [1]. *Center*: Alignment-driven collective motion of active rollers. [2] *Right*: Active droplets forming transient lanes [3].

However, the path to achieve a full understanding of the self-organization of active materials into complex patterns is still at its first steps. Much work has been done

by theorists to model simple, single-component systems, but not much is known so far regarding multi-component active matter. Research in this direction is crucial if we want to tackle non-idealised situations like the ones encountered in biology, where heterogeneity is always present.
The aim of this project is to provide a methodology for modelling N-species active mixtures. Starting from microscopic Langevin dynamics, we want to carry out a bottom-up approach to derive macroscopic descriptions of the systems. Eventually, our goal is to determine the forms of organization that can emerge at the large-scale level, relating them to the microscopic interactions at play. Bridging the gap between the microscopic world and the emergent macroscopic organization will allow us to decipher the principles for assembling increasingly complex structures.

1.1.1 Run-and-tumble particles

Throughout this work, we shall focus on a specific model of active dynamics: *run-and-tumble particles* (RTPs). This class of particles has been extensively studied in the literature of monodisperse active systems and it has been especially employed to describe the swimming dynamics of *E. Coli*. For sake of clarity, we shall focus on two-dimensional systems, but the generalization of our results to higher dimensions is straightforward.

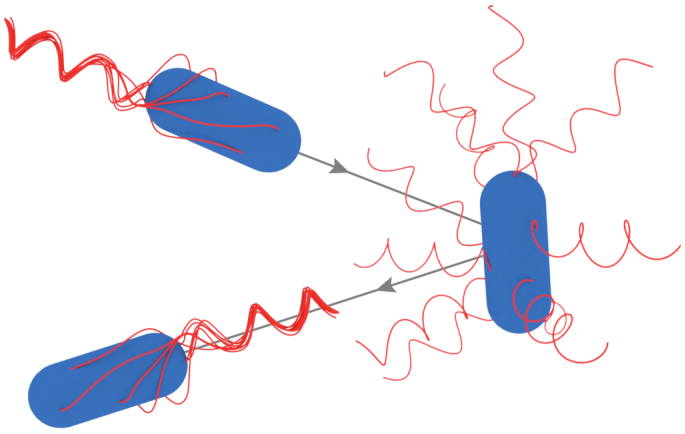

Figure 1.4: Swimming of an *E. Coli* bacterium. Following a tumbling event, the bacterium re-orients, then resumes running in a new, random direction. Picture form [6].

The model is as follows: each particle moves in a constant direction, parametrized by an angle θ, at a self-propulsion speed v. With rate α, a stochastic tumbling event occurs and the bacterium abruptly stops. Once the particle is in the stopping state, it can return to the running state with rate β. When this occurs, the orientation of

the particle changes instantaneously from $\theta \to \theta'$, where θ' is drawn from a uniform distribution over $[0, 2\pi)$.
Whenever β is finite, the residence time in the stopping state is nonzero; we refer to this case as *finite-duration* tumble. In the $\beta \to +\infty$ limit, instead, we are dealing with *instantaneous tumbles*. For simplicity, we will focus on the latter case.
This choice is well motivated in the case of *E. Coli*, where the stopping-to-running transition occurs with a typical rate $\beta \sim 10$ Hz, that is much higher than the tumbling one $\alpha \sim 1$ Hz.

The dynamics will thus read:

$$\dot{\mathbf{r}}(t) = v\,\mathbf{u}(\theta)\eta(t) \qquad \mathbf{u}(\theta) = \begin{pmatrix}\cos\theta \\ \sin\theta\end{pmatrix} \tag{1.1}$$

$$\theta \to \theta' \qquad \text{stochastically with rate } \alpha, \quad \theta' \sim \mathbb{I}_{[0,2\pi)} \tag{1.2}$$

1.1.2 Quorum-sensing interactions

To provide a description of active systems that is close to actual biological situations, it is necessary to consider how each particle interacts with its environment and with its neighbours. In a large class of systems, from E. Coli [7] to algae [8] and epithelial cells [9], tactic behaviours emerge as a mechanism to regulate particles' motility. In the specific case of bacteria, each particle can adapt its self-propulsion speed v and its tumbling rate α according to the concentration gradients of chemical substances in the environment, such as food or toxins (*chemotaxis*). Following the lines of J. O'Byrne and J. Tailleur [10], gradients of a chemical field $c(\mathbf{r})$ can impinge on the motility:

$$v = v_0 - v_1\mathbf{u}\cdot\nabla c \qquad \alpha = \alpha_0 + \alpha_1\nabla c \tag{1.3}$$

where $\mathbf{u}$ is the usual orientation unit vector. Positive α_1, v_1 bias the particle's motion towards lower values of c (chemorepellent).
In this study, we focus on a second class of particles, that are sensitive to the chemical field itself rather than to its gradients. Such particles are said to undergo *quorum sensing* (QS). This corresponds to setting $\alpha_1, v_1 = 0$ in (1.3), but letting α_0, v_0 be functions of $c(\mathbf{r})$.
In bacterial systems, chemicals are produced and consumed by the particles themselves, leading to a coupling between the bacterial and chemical dynamics. A natural model [10] for the chemical field dynamics is then to consider diffusion, degradation

and production by the bacteria:

$$\partial_t c(\mathbf{r}) = D_c \Delta c - \lambda c - \beta \sum_i \delta(\mathbf{r} - \mathbf{r_i}) \tag{1.4}$$

where D_c is the chemical diffusivity, λ is the rate of degradation in the environment, and β the production rate by bacteria. Assuming that the chemical dynamics is much faster than the particle's, we can set $\partial_t c = 0$ in (1.4) and obtain the concentration field $c(\mathbf{r})$ as a functional of the particle density $\rho(\mathbf{x})$:

$$c(\mathbf{r}) = \int \mathrm{d}^2 y \, G(\mathbf{x} - \mathbf{y}) \, \rho(\mathbf{y}) \tag{1.5}$$

where $G(\mathbf{r})$ is the Green function solution of $(D_c \Delta - \lambda) G(\mathbf{r}) = \beta \delta(\mathbf{r})$.

Summing up: each bacterium adjusts its motility according to the chemical field $c(\mathbf{r})$; the concentration field $c(\mathbf{r})$, in turn, depends on the bacterial density field $\rho(\mathbf{y})$ through (1.5). All-in-all, we can forget the chemical field, incorporating its role into an effective interaction between bacteria, namely *quorum-sensing interaction*.
In a mixture of N bacterial strains, strain i will be allowed to interact in a specific way with strain j. In practice, α_i and v_i are thus functionals of all the density fields $[\vec{\rho}] = [\rho_1, \ldots, \rho_N]$.

Let us now recap our model. Let $\mathbf{r}_{i,X}$ be the position of the i-th particle of species X. In our notation for the microscopic dynamics, we let X indicate the species label: $X \in \{1, \ldots, N\}$.
We also introduce $\mathbf{u}_i = (\cos\theta_i, \sin\theta_i)$, the 2D unit vector describing the instantaneous orientation of particle i. Finally, we take into account the presence of an external translational noise term in the dynamics, with diffusivity D_t.
The stochastic dynamics of particle i is thus expressed as:

$$\dot{\mathbf{r}}_{i,X}(t) = v_X(\mathbf{r}_i, [\vec{\rho}]) \, \mathbf{u}_i(\theta) + \sqrt{2D_t}\eta_i(t) \tag{1.6}$$

$$\eta_i : \quad \text{Gaussian white noise with } \langle \eta_i(t) \eta_j(t') \rangle = \delta(t - t') \tag{1.7}$$

$$\theta \to \theta' \quad \text{stochastically with rate } \alpha_X(\mathbf{r}, [\vec{\rho}]), \quad \theta' \sim \mathbb{I}_{[0,2\pi)}, \tag{1.8}$$

where we have made explicit the dependence of each species' motility parameters on the density fields, on the position of particle i in space, and on the particle's species X.

1.1.3 Single-component systems

Monodisperse active systems have been extensively studied from both theoretical and experimental points of view [11], [12]. Different types of microscopic interactions can give rise to rich behaviours at the macroscopic scale, from phase separation in the absence of attractive forces to alignment-induced collective motion. In this study, we restrict our attention to *scalar active systems*, made up of spherical particles with isotropic and nonaligning interactions.
In the context of RTPs, persistence can give rise to new phenomena with respect to passive systems, such as accumulation at boundaries or gravitational collapse of sedimenting particles [13], [14]. Furthermore, in the case where QS-interaction is included, J. Tailleur and M. Cates [15] first observed liquid-gas coexistence in the absence of attractive forces, following the so-called *motility-induced phase separation* (MIPS). MIPS occurs when the self-propulsion speed v is a sufficiently rapidly decreasing function of the local density ρ, that is to say when crowding causes particles to slow down at high density. This is a first example of how activity can lead to a simple form of macroscopic organization.

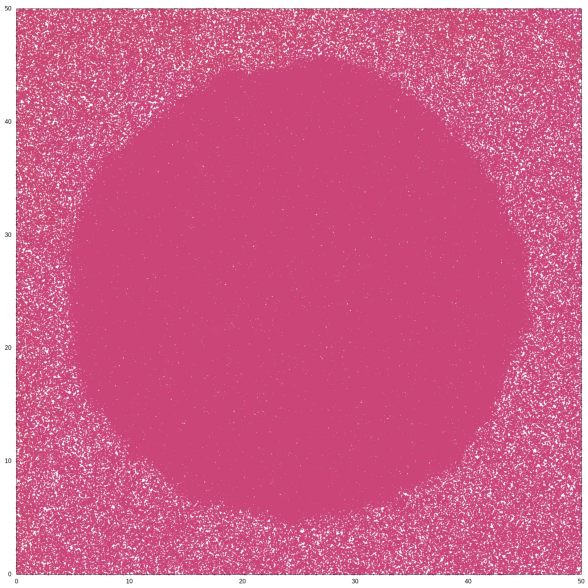

Figure 1.5: Motility-induced phase separation in a system of quorum-sensing RTPs: snapshot from a molecular dynamics simulation performed with our code.

Nevertheless, monodispersity imposes strong limits on the complexity that can be achieved in terms of large-scale organization. In order to obtain more complex self-assembling structures, it is necessary to go beyond monodisperse active matter and consider multi-component systems.

1.1.4 Multi-component active systems: relevance and challenges

Heterogeneity is ubiquitous in biological systems: from the intra-cellular environment to microbial population in the gut, to epithelial cells in animals, diversity is the basis of complex organization. From this point of view, multi-component active matter is thus relevant to describe biological systems at all scales.

A first study on the macroscopic organization of bacterial mixtures interacting via QS was published in Nature Physics in 2020 [16]. In this work, two strains of *E. Coli* were engineered to cross-regulate each other's motility and left to grow in a Petri dish. Depending on the type of cross-interaction, whether it was mutual inhibition or mutual activation of motility, two different emergent patterns were observed, namely *mixed* or *demixed* concentric rings (Figure 1.6). In the same paper, these observations were explained by A. Curatolo and co-workers in terms of binary mixtures of RTPs with finite-duration tumbles. Through a coarse-graining procedure, microscopic cross-interactions were related to the mixed or demixed phase at the large-scale level. This is the first example, in the context of active mixtures, of a full theory that accounts for macroscopic patterns starting from a microscopic description.

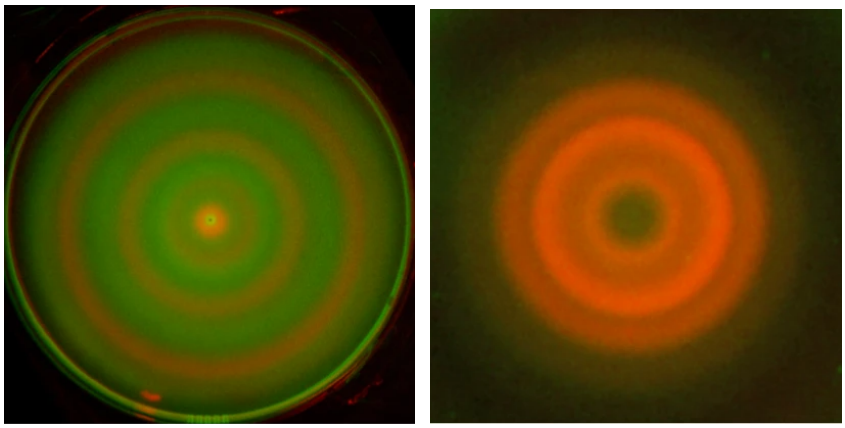

Figure 1.6: In the experiment described in [16], two strains of *E. Coli* are engineered to mutually activate/inhibit each other's motility. Each strain is marked with a different fluorescent marker, either green or red. (*Left*) Mutual activation of motility leads to spatially-separated rings of the two strains, i.e. demixing. (*Right*) Mutual inhibition leads to macroscopic colocalization of the two strains, i.e. mixing.

Nevertheless, the kind of patterns explained by this theory do not cover the entire phenomenology of binary active mixtures. R. Golenstanian et al. [17] tackled the N-component problem starting from a phenomenological Cahn-Hilliard theory for the density fields. From simulations, they proved the existence of traveling patterns in binary mixtures, going beyond the static patterns predicted by A. Curatolo [16]. (Figure 1.7)

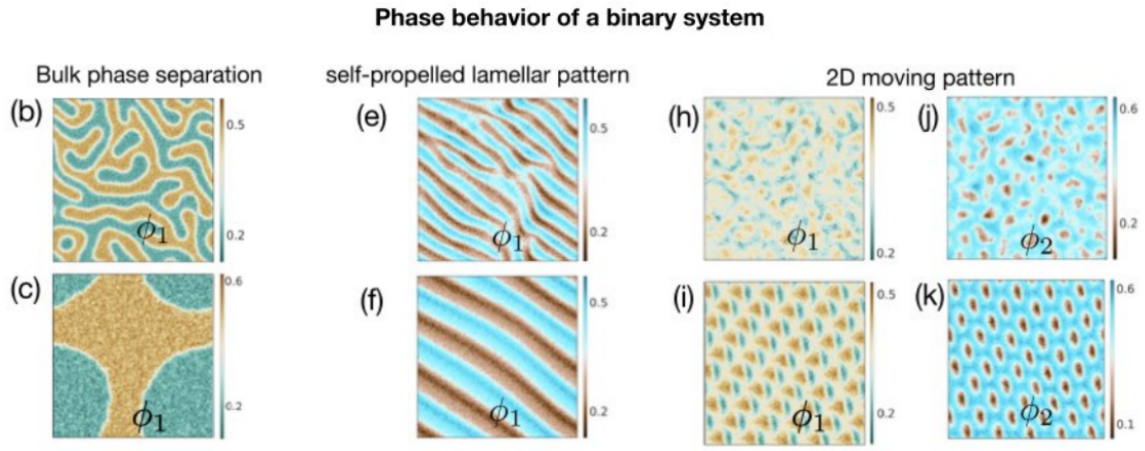

Figure 1.7: Simulations of a phenomenological theory reveal a rich phase behaviour for binary systems, from static to dynamic patterns. [17]. In each panel, a single component ϕ_i of the mixture is depicted. Colorcode corresponds to the density scale for the component that is displayed.

These observations are the starting point of my internship: can we classify generally all the macroscopic phases observable in mixtures of quorum-sensing active particles, and can we build a general framework to do so? Answering these questions will be the goal of my Ph.D. Here, I describe the first step I made in this direction.

1.2 Outline of the thesis

The aim of this work is to study the phenomenology of active mixtures and to understand the role of microscopic parameters in the emergent large-scale organization. To achieve this goal, we will provide a set of numerical and analytical tools to tackle the general N-component problem, comparing simulations with analytical predictions.

The thesis is structured as follows:

- At the beginning of chapter 2, we study the rich phase behaviour resulting from microscopic simulations of binary systems. In order to explain the emergence of the observed phases, we coarse-grain the microscopic theory to obtain the macroscopic dynamics of the density fields. Via a mean-field treatment, we can eventually get a phase-diagram for the case of binary mixtures.

- In chapter 3, we focus on the possibility of an equivalence between macroscopic active mixtures and passive equilibrium systems. If such a mapping exists, time-reversal symmetry is present at the macroscopic level. Can we then pinpoint the main features that distinguish an equilibrium pattern from a non-equilibrium one? This part is fundamentally methodological, and it mostly relies on tools of functional calculus.
- Finally, in chapter 4 we give some perspectives on the future of this project and its possible scope of applications.

The analytical part heavily relies on tools that are traditionally used in theoretical active matter: stochastic calculus, coarse-graining techniques, linear analysis of PDEs. As regards the numerics, I have developed a `C` code from scratch to simulate the coupled Langevin dynamics of N active particles belonging to K different classes. Data analysis was carried out mostly in `Mathematica` and `Python`.

Chapter 2

Phenomenology of active mixtures

In this chapter, we illustrate the emergent macroscopic phases in active mixtures, with a special focus on the two-component case. Starting from molecular dynamics simulations, we try to understand how the interplay between microscopic ingredients generates different large-scale behaviours. Special focus will be put on dynamic patterns, that have not been observed so far in microscopic simulations of binary mixtures. As far as static patterns are concerned, instead, we will present a new interesting phenomenology, showing that self-inhibition can induce mixing or demixing even when cross-interactions are weak.
In the second part of the chapter, we present an analytical procedure to coarse-grain the multi-species RTP microscopic dynamics up to the level of the density-field dynamics. Here, calculations mostly rely on those performed by A. Curatolo in [16] and [18], with an adaptation to the case of instantaneous tumbling.
Once we have the stochastic field dynamics, our goal is to study the kind of patterns it can give rise to. Our approach is based on a mean-field treatment. Besides, we assume locality of QS-interactions, imposing the dependence of microscopic parameters only on the local values of the density fields. Within this framework, we study how a small, linear perturbation can affect a homogeneous configuration. Despite the number of approximations, the theory will provide the key ingredients to explain the emergence of the phases observed in the simulations, and we will eventually be able to compare the mean-field phase diagram with our numerical results.

2.1 Simulations of binary systems

In order to observe which type of macroscopic patterns can emerge from the RTP-mixture dynamics, I developed from scratch a `C` code to simulate the N-species cou-

pled Langevin dynamics. We performed off-lattice molecular dynamics (MD) simulations for a binary system of RTPs in 2D. The details of the implementation are illustrated in Appendix A, together with the test of the code. Here, instead, we focus on the results of simulations for two species.

Two-species $\{A,B\}$ of RTPs are considered, interacting via QS within a finite radius d. One particle of species X modulates its velocity based on the local density of its species $\rho_{i,X}$ and the other $\rho_{i,Y}$, according to a sigmoid-like function:

$$v_{i,X} = v_{0,X} \exp\left(-K_X \arctan\left(\frac{\rho_{i,X}-\rho_M}{L_f}\right) + J_X^Y \arctan\left(\frac{\rho_{i,Y}-\rho_M}{L_f}\right)\right) \tag{2.1}$$

Here, K_X controls self-interaction for species X: a positive value of K_X corresponds to self-inhibition of motility, while a negative one is associated with self-activation. J_X^Y quantifies how a particle of species X is affected by the presence of another one of different species Y: $J_X^Y > 0$ means that the velocity of an X-particle is increased by the presence of Y-particles in the nearby, i.e. cross-activation of X by Y. On the contrary, cross-inhibition of X by Y is associated with $J_X^Y < 0$.
The use of sigmoidal functions to model QS-regulation of motility is a common choice in the literature [19], with biological grounds in experiments on *E. Coli* [20], (Figure 2.1). The specific choice of (2.1) is mainly due to analytical treatability, but numerical results are indeed robust over different sigmoid-like functions.

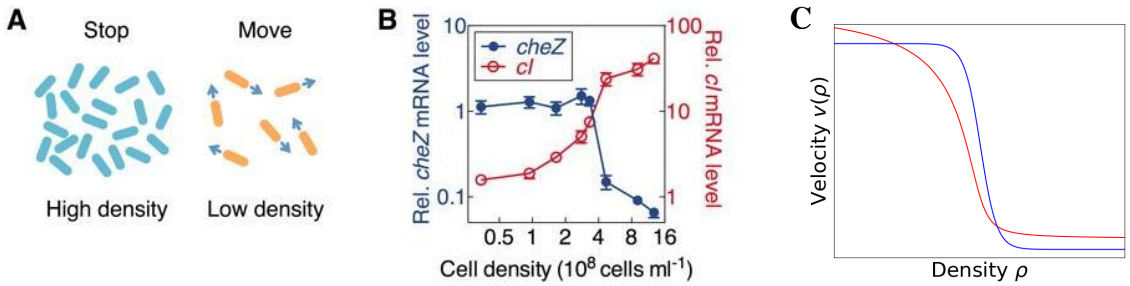

Figure 2.1: (**A**) Cartoon of bacterial motility as a function of density. (**B**) Relative *cheZ* and cI mRNA level in *E. Coli* strain as a function of cell density in bulk culture. *cheZ* is a molecular complex that is responsible for bacterial motility, and whose deletion causes the bacterium to incessantly tumble. The decreasing level of *cheZ* as a function of cell density is therefore associated with a decreasing motility [20]. (**C**) Two examples of sigmoidal functions $v(\rho)$: in red, $v(\rho) = v_0 \exp(-\arctan(\rho-\rho_0))$; in blue, $v(\rho) = v_0[1-\tanh(\rho-\rho_0)]$. Despite quantitative differences, the qualitative shape of these curve is analogous.

In our simulations, we vary the strength and sign of interactions $\{K_X, J_X^Y\}$, in order to observe different phases. Besides, we focus on the case $K_A = K_B = K$, so as to reduce the space of parameters to be explored. Further details on the choice of parameters can be found in Appendix A.

Dynamic patterns

One of the most interesting observation is the emergence of self-propelling bands, reminiscent of those obtained by R. Golenstanian et al. in [17] in their phenomenological study, despite important morphological differences. This phase is observed in a regime of parameters where J_A^B and J_A^B have opposite signs, corresponding to non-reciprocal cross-interactions. The two species remain spatially separated while one chases after the other (Figure 2.2).
In the presence of self-inhibition ($K > 0$), starting from small values $J_A^B = -J_B^A$ and increasing gradually the cross-interaction strength, we observe a smooth transition from slow, floating clusters up to proper bands (Figure 2.3).
Plus, simulations show that bands are robust with respect to the suppression of self-interaction K. Nonetheless, wavefronts tend to become less clearcut and more fuzzy (Figure 2.2). Finally, when $K = 0$, floating clusters are not observed.

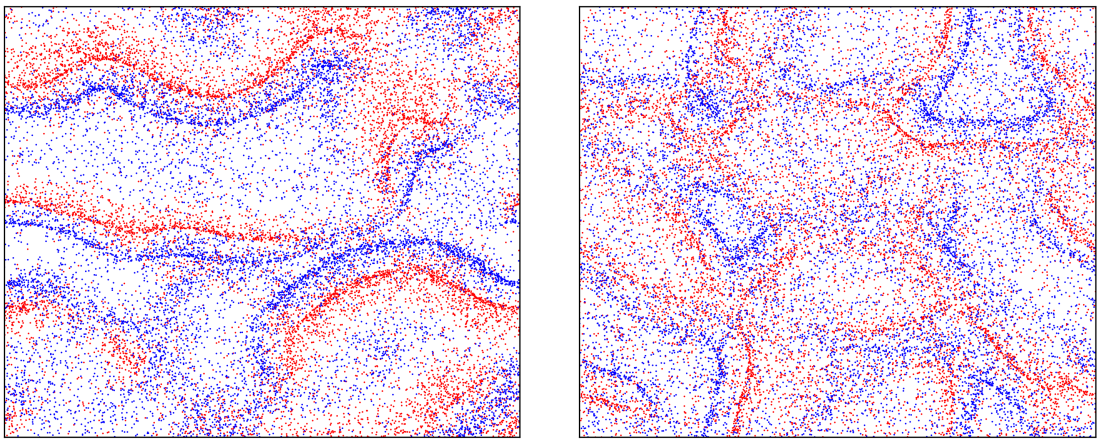

Figure 2.2: Self-propelling bands observed in simulations. *Left*: Bands in the presence of self-inhibition $K = 1$, $|J| = 1$. *Right*: Bands in the absence of self-inhibition $K = 0$, $|J| = 1$.

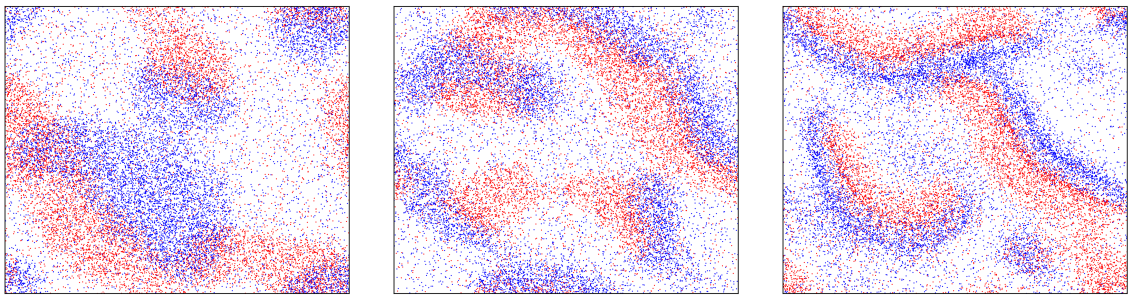

Figure 2.3: Smooth transition from slow, floating clusters to self-propelling bands, increasing the cross-interaction strength. From left to right, $|J| = 0.1$, $|J| = 0.4$, $|J| = 0.6$. Self-inhibition is constant in all simulations: $K = 1$.

Static patterns

Mixing

If we take both cross-interactions J_A^B, J_B^A of negative sign, what we observe is macroscopic phase separation accompanied by *mixing*, i.e. a phase where the two different species cluster together in a dense slab $\{\rho_A^h, \rho_B^h\}$ in coexistence with a gaseous bulk $\{\rho_A^l, \rho_B^l\}$. Qualitatively, negative cross-interactions imply a slow-down of one species in the presence of the other, thus leading to accumulation of A and B in the same spatial region (Figure 2.4).
In this scenario, self-inhibition can play a relevant role by favouring mixing even in the presence of weak cross-interactions. Indeed, if we set $J_A^B = J_B^A$ to a small value, then we increase self-inhibition K, we observe a transition from homogeneous to mixed phase (Figure 2.6). This result sheds new light on the role of self-inhibition to induce mixing or demixing, a phenomenon that has not been examined in the literature so far.
Finally, an interesting dynamics emerges when one cross-interaction is much weaker than the other $|J_A^B| \ll |J_B^A|$. In this case, simulations highlight a macroscopic separation of timescales, where the dynamics of species A is fast, while B is fundamentally frozen (Figure 2.7). In particular, when B-particles meet a group of A-particles, the former abruptly stop due to the strong self-inhibition, while the latter are just slightly slowed down. This leads, as observed in simulations, to the formation of sharp B-interfaces around A-clusters. The dynamics of such interfaces is entirely driven by the fast A-particles' dynamics.

Demixing

Finally, when cross-interactions J_A^B, J_B^A are both positive, we observe macroscopic phase separation in presence of *demixing*, i.e. the two different species form spatially-separated macroscopic clusters (Figure 2.5). At a microscopic level, positive J causes one species to accelerate in the presence of the other.
Again, increasing self-inhibition can lead to the emergence of a demixed phase even in presence of weak cross-interactions.
Analogously to the mixing case, when the strengths of the cross-interaction terms is very different we observe a separation of timescales in the macroscopic dynamics, with sharp interfaces that are driven by the fast-moving species (Figure 2.8).

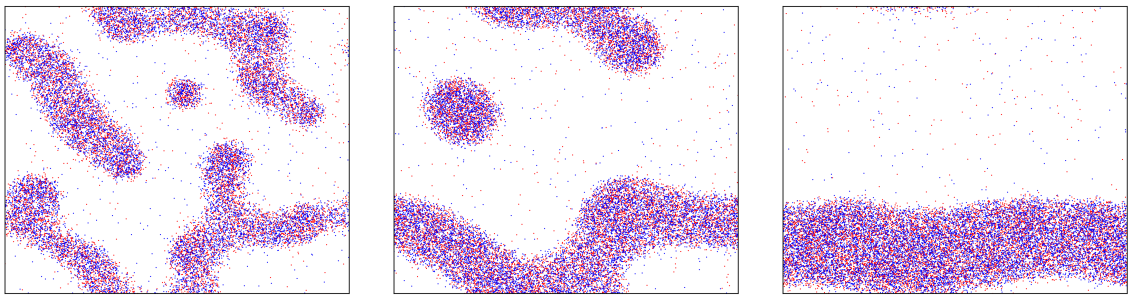

Figure 2.4: Successive snapshots of static mixing of a binary mixture for $J_A^B = J_B^A = -1$, self-inhibition $K = 1$. *Left*: Simulation at $t = 10$. *Center*: Simulation at $t = 100$. *Right*: Simulation at $t = 1000$.

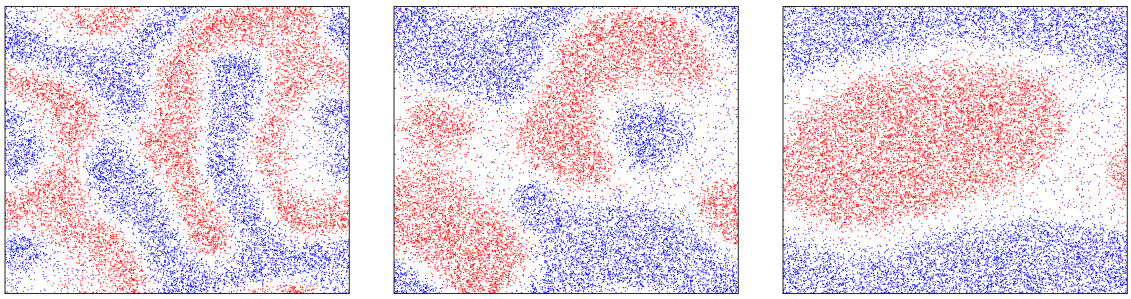

Figure 2.5: Successive snapshots of static demixing of a binary mixture for $J_A^B = J_B^A = 1$, self-inhibition $K = 1$. *Left*: Simulation at $t = 10$. *Center*: Simulation at $t = 100$. *Right*: Simulation at $t = 1000$.

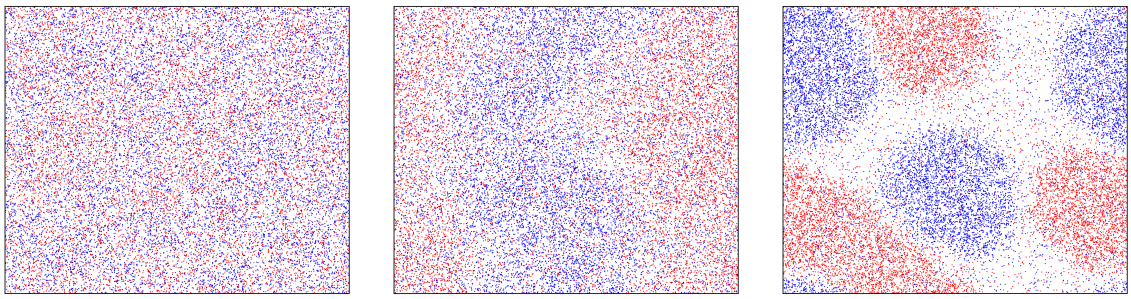

Figure 2.6: Transition from homogeneous to demixed phase in a binary mixture, induced by self-inhibition. In the figures, three snapshots of different simulations where we vary the strength of self-interactions K. The two strains are weakly mutually activating, with $J_A^B = J_B^A = 0.1$. We observe how self-inhibition can induce demixing even in presence of weak cross-interactions. *Left*: Simulation at $K = 0.3$. *Center*: Simulation at $K = 0.5$. *Right*: Simulation at $K = 1$.

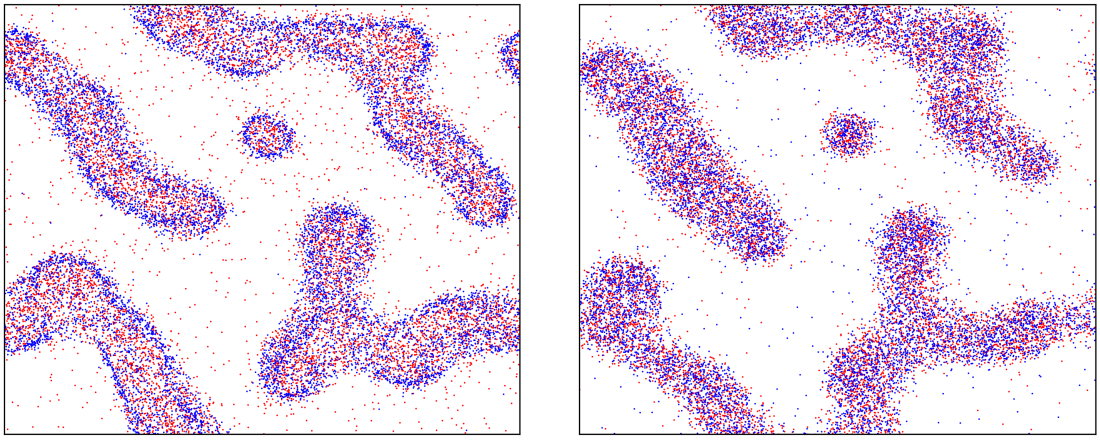

Figure 2.7: Comparison between two snapshots of mixing with (*left*) and without (*right*) macroscopic time-scale separation. In the first case, cross-inhibition of blue (B) particles by red (A) is much stronger than the converse ($J_B^A = 3$, $J_A^B = -0.5$). This leads to a frozen state of the blue particles when they meet the red ones, resulting in sharp interfaces around liquid clusters. The dynamics of such interfaces is exclusively driven by the motion of fast red particles in the simulation.

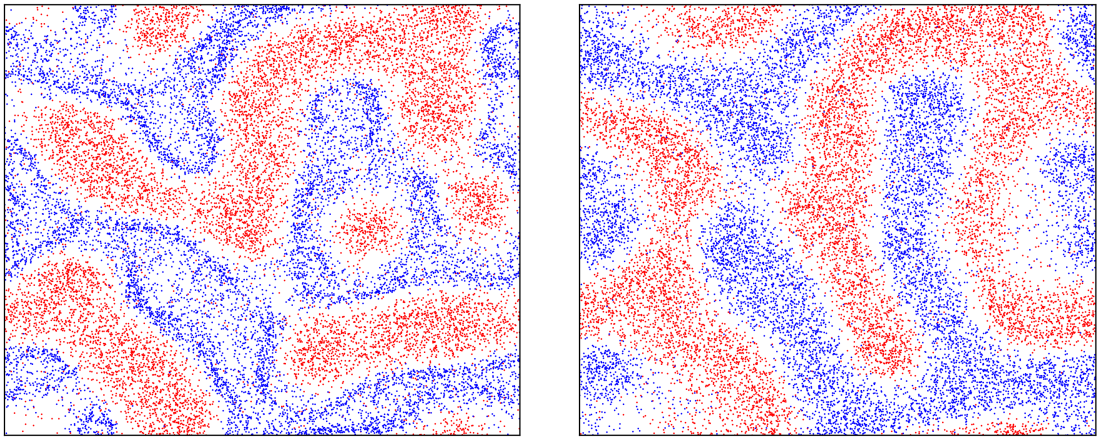

Figure 2.8: Comparison between two snapshots of demixing with (*left*) and without (*right*) macroscopic time-scale separation. In the first case, cross-activation of blue (B) particles by red (A) ones is much stronger than the converse ($J_B^A = 3$, $J_A^B = 0.5$).

2.2 From micro to macro

In the previous section, we have illustrated three collective macroscopic behaviours for a binary system of RTPs. The aim is now to provide a physical explanation to these numerical observations by bridging the gap from the microscopic dynamics to the emergent large-scale patterns.
First, we will coarse-grain our theory, starting from the dynamics of the microscopic degrees of freedom $\{\mathbf{r}_i, \theta_i\}$ to build the one of the density fields $[\rho_1, \dots, \rho_N]$. Once we have a stochastic field theory for the densities, we will try to explain, via linear stability arguments, which types of patterns can be formed.

2.2.1 N-species coarse-graining

Coarse-graining techniques for RTPs have been widely described in the active matter literature [14], with application in several contexts like bacterial chemotaxis [10], aligning particles, binary mixtures [16]. In this work, we extend the treatment by A. Curatolo et al. [16] to N species of RTPs with instantaneous tumbles.
In the dynamics (1.8), motility parameters depend explicitly on the density fields, coupling the motion of all particles. However, since density fields $\{\rho_i\}$ are conserved fields, their evolution occurs on a large timescale, which we expect to be diffusive $\tau \sim L^2$. When studying the small-scale particle dynamics, we can therefore assume the density fields to be fixed (*frozen-field approximation*). This solution maps the microscopic system from interacting RTPs to non-interacting ones, albeit with motility parameters that depend on the particle's position:

$$\alpha_X, v_X(\mathbf{r_i}, [\vec{\rho}]) \quad \longrightarrow \quad \alpha, v(\mathbf{r_i}) \tag{2.2}$$

We can now try to coarse-grain out the orientational degree of freedom for the dynamics of a single particle. Let $\mathscr{P}(\mathbf{r}, \theta; t)$ be the probability of finding one particle at position $\mathbf{r}$ with orientation θ at time t. The associated master equation reads:

$$\partial_t \mathscr{P}(\mathbf{r}_i, \theta_i) = -\nabla_{\mathbf{r}_i} \cdot [\, v(\mathbf{r}_i)\, \mathbf{u}(\theta_i) \mathscr{P} - D_t \nabla_{\mathbf{r}_i} \mathscr{P}\,] - \alpha \mathscr{P}(\mathbf{r}_i, \theta_i) + \frac{\alpha}{2\pi} \int \mathrm{d}\theta'\, \mathscr{P}(\mathbf{r}_i, \theta')\,, \tag{2.3}$$

where, in addition to the usual drift and diffusion currents, gain and loss terms due to tumbles are present. If we expand $\mathscr{P}$ in Fourier harmonics:

$$\mathscr{P}(\mathbf{r}, \theta, t) = \frac{1}{2\pi} \sum_{n=-\infty}^{+\infty} C_n(\mathbf{r}, t)\, e^{in\theta} \tag{2.4}$$

we can use (2.3) to write the time-evolution of the $C_n(\mathbf{r},t)$. In particular, we see that the zeroth-order harmonics:

$$C_0(\mathbf{r},t) = \int_0^{2\pi} \mathrm{d}\theta\, P(\mathbf{r},\theta,t) \tag{2.5}$$

corresponds to the marginalized probability of finding a particle in position $\mathbf{r}$ at time t, irrespective of its orientation.
Starting from eq. (2.3) one gets:

$$\partial_t C_0 = -\nabla_{\mathbf{r}_i}\cdot\left[\frac{v}{2}\left(\begin{pmatrix}1\\-i\end{pmatrix}C_{+1}+\begin{pmatrix}1\\i\end{pmatrix}C_{-1}\right)-D_t\nabla_{\mathbf{r}_i}C_0\right] \tag{2.6}$$

$$\partial_t C_{\pm1} = -\nabla_{\mathbf{r}_i}\cdot\left[\frac{v}{2}\left(\begin{pmatrix}1\\\mp i\end{pmatrix}C_{\pm2}+\begin{pmatrix}1\\\pm i\end{pmatrix}C_0\right)-D_t\nabla_{\mathbf{r}_i}C_{\pm1}\right]-\alpha C_{\pm1} \tag{2.7}$$

$$\partial_t C_{\pm2} = -\nabla_{\mathbf{r}_i}\cdot\left[\frac{v}{2}\left(\begin{pmatrix}1\\\pm i\end{pmatrix}C_{\pm3}+\begin{pmatrix}1\\\mp i\end{pmatrix}C_{\pm1}\right)-D_t\nabla_{\mathbf{r}_i}C_{\pm2}\right]-\alpha C_{\pm2} \tag{2.8}$$

From the above equations, we note that the dynamics of each harmonics is coupled also to higher-order ones. It is thus necessary to impose a closure to the hierarchy of equations. In order to do so, we observe from eq. (2.6) that C_0 is a conserved field, hence it evolves at a slow scale. On the contrary, $C_{\pm1}$ and $C_{\pm2}$ undergo both a large-scale diffusive dynamics ($\sim\nabla_{\mathbf{r}}$) and a fast exponential relaxation (with finite relaxation time $\sim\alpha^{-1}$). In the limit of large system size $L\to\infty$, we can therefore assume that $C_{\pm1}$, $C_{\pm2}$ relax istantaneously to values enslaved to that of $C_0(\mathbf{r},t)$. Subsequently, one can rewrite eqs. (2.7, 2.8) as:

$$\partial_t C_{\pm2}=0 \quad\Rightarrow\quad \alpha C_{\pm2} = -\nabla_{\mathbf{r}_i}\cdot\left[\frac{v}{2}\left(\begin{pmatrix}1\\\pm i\end{pmatrix}C_{\pm3}+\begin{pmatrix}1\\\mp i\end{pmatrix}C_{\pm1}\right)-D_t\nabla_{\mathbf{r}_i}C_{\pm2}\right] \tag{2.9}$$

$$\partial_t C_{\pm1}=0 \quad\Rightarrow\quad \alpha C_{\pm1} = -\nabla_{\mathbf{r}_i}\cdot\left[\frac{v}{2}\left(\begin{pmatrix}1\\\mp i\end{pmatrix}C_{\pm2}+\begin{pmatrix}1\\\pm i\end{pmatrix}C_0\right)-D_t\nabla_{\mathbf{r}_i}C_{\pm1}\right] \tag{2.10}$$

Finally, we can plug eqs. (2.9, 2.10) into the dynamics of the zeroth harmonics (2.6). In order to close the equations, we truncate the expansion including terms up to $\mathscr{O}(\nabla^2)$. This is the so-called *diffusion-drift approximation*, which relies on the fact that large-scale hydrodynamic modes are assumed to satisfy $\nabla^k\sim\frac{1}{L^k}$. While this is true for relaxations around homogeneous states, this approximation is expected to break down when phase separation gets in, and we should keep in mind this limitation.
Finally, we obtain a mesoscopic Fokker-Planck equation for the marginalized probability $C_0(\mathbf{r_i},t)$:

$$\partial_t C_0 = -\nabla_{\mathbf{r}_i}\cdot[\mathbf{V}C_0 - D\nabla_{\mathbf{r}_i}C_0] \tag{2.11}$$

where we introduced the *mesoscopic drift velocity* $\mathbf{V}$ and *mesoscopic diffusivity* D:

$$\mathbf{V} = -\frac{v\nabla v}{2\alpha} \qquad D = \frac{v^2}{2\alpha}+D_t \tag{2.12}$$

Now that we have discarded the orientational degrees of freedom, we can study the large-scale interacting dynamics by restoring the dependence on the density fields. In particular, we can associate to the Fokker-Planck equation (2.11) a corresponding *mesoscopic Ito-Langevin equation* for a particle of species X:

$$\dot{\mathbf{r}}_i = \mathbf{V}_X(\mathbf{r}_i,[\vec{\rho}]) + \nabla_{\mathbf{r}_i} D_X(\mathbf{r}_i,[\vec{\rho}]) + \sqrt{2D_X(\mathbf{r}_i,[\vec{\rho}])}\,\xi(t) \tag{2.13}$$

$$\xi \;:\; \text{Gaussian white noise with } \langle \xi_i(t)\xi_j(t')\rangle = \delta_{i,j}\delta(t-t') \tag{2.14}$$

where we observe that strain labels X have been re-introduced. Eqs. (2.13) and (2.14) are where the mesoscopic theories of multi-component systems of RTPs start to differ from the single-component case studied in [21].

2.2.2 From mesoscopic dynamics to fluctuating hydrodynamics

As a final step of our coarse-graining, we want to write down the equations for the dynamics of the density fields $[\rho_1,\dots,\rho_N]$ starting from the mesoscopic Langevin equation (2.13). Here, the derivation is a straightforward generalization of the Dean procedure used for single-component systems (see for example [14]). The interested reader can find the full details of the calculation in Appendix B.

We define the density of species i as:

$$\rho_i(\mathbf{r},t) = \sum_{k:\,\mathrm{Label}(k)=i} \delta(\mathbf{r}-\mathbf{r}_k(t)) \tag{2.15}$$

The macroscopic field equation for ρ_i is then:

$$\boxed{\dot{\rho}_i(\mathbf{r}) = -\nabla\cdot\left[\mathbf{V}_i(\mathbf{r},[\vec{\rho}])\rho_i(\mathbf{r}) - D_i(\mathbf{r},[\vec{\rho}])\nabla\rho_i(\mathbf{r}) + \sqrt{2D_i\rho_i}\,\Lambda\right]} \tag{2.16}$$

where:

$$D_i = \frac{1}{2}\frac{v_i^2(\mathbf{r},[\vec{\rho}])}{\alpha_i(\mathbf{r},[\vec{\rho}])} + D_t(\mathbf{r},[\vec{\rho}]) \qquad i\in\{1,\dots,N\} \tag{2.17}$$

$$\mathbf{V}_i = -\frac{1}{2}\frac{v_i\nabla v_i(\mathbf{r},[\vec{\rho}])}{\alpha_i(\mathbf{r},[\vec{\rho}])} = -D_i\nabla\log(v_i(\mathbf{r},[\vec{\rho}])) \tag{2.18}$$

and Λ is a Gaussian white-noise field with:

$$\langle\Lambda\rangle = 0 \qquad \langle\Lambda_\alpha(\mathbf{r},t)\Lambda_\beta(\mathbf{r}',t)\rangle = \delta_{\alpha,\beta}\delta(\mathbf{r}-\mathbf{r}')\delta(t-t') \tag{2.19}$$

2.3 Collective behaviours: linear stability analysis at mean-field level

Once that a macroscopic theory for the density fields has been derived, we can try to determine the forms of organization that will emerge at the large-scale level. The idea of this section is to provide some analytical predictions, with a special focus on the $N = 2$ case. In order to proceed with calculations, a certain number of approximations will be necessary:

- *Mean field*: We consider the evolution of the average field $\langle\rho\rangle$, assuming that: $\langle f(\rho)\rangle \approx f(\langle\rho\rangle)$ for any function f entering the dynamics (2.16)
- *Locality of QS-interactions*: Microscopic motility parameters $v(\mathbf{r},[\rho_i]), \alpha(\mathbf{r},[\vec{\rho}])$ will be assumed to be local functions of the densities $\{\rho_i(\mathbf{r})\}$ only, instead of more generic, non-local functionals.

The idea is to consider a homogeneous density profile:

$$\vec{\rho}_0 = \{\rho_{1,0}, \rho_{2,0}, \dots, \rho_{N,0}\} \tag{2.20}$$

and see how it can be unstabilized by a small, linear perturbation $\delta\vec{\rho}$.
The mean-field equations for the active mixture read:

$$\dot{\rho}_i(\mathbf{r}) = -\nabla\cdot[\mathbf{V}_i(\mathbf{r},[\vec{\rho}])\rho_i(\mathbf{r}) - D_i(\mathbf{r},[\vec{\rho}])\nabla\rho_i(\mathbf{r})] \tag{2.21}$$

$$D_i = \frac{1}{2}\frac{v_i^2(\mathbf{r},[\vec{\rho}])}{\alpha_i(\mathbf{r},[\vec{\rho}])} \qquad i\in\{1,\dots,N\} \tag{2.22}$$

$$\mathbf{V}_i = -\frac{1}{2}\frac{v_i\nabla v_i(\mathbf{r},[\vec{\rho}])}{\alpha_i(\mathbf{r},[\vec{\rho}])} = -D_i\nabla\log v_i(\mathbf{r},[\vec{\rho}]) \tag{2.23}$$

Let $\rho_i = \rho_{i,0} + \delta\rho_i$. Assuming locality of the microscopic velocity v_i and tumbling rate α_i, we can expand (2.21) to linear order in $\delta\vec{\rho}$. The derivation is not complicated but the notations rapidly become cumbersome, so here we will present only the results, leaving the details to Appendix C.1.
Eventually, if we define the *excess local chemical potentials* $\mu_i \equiv \log v_{i,0}$, the linear expansion of the mean-field equation can be shown to be:

$$\delta\dot{\rho}_i = D_{i,0}\,\rho_{i,0}\left[\sum_{j=1}^{N}\partial_j\mu_i\,\nabla^2\delta\rho_j + \frac{1}{\rho_{i,0}}\nabla^2\delta\rho_i\right] + \mathscr{O}(\delta\rho^2) \tag{2.24}$$

Introducing the Fourier transform of the density perturbation:

$$\delta\vec{\rho}_{\mathbf{q}} = \int d^2x\, e^{-i\mathbf{q}\cdot\mathbf{x}}\, \delta\vec{\rho}(\mathbf{x}) \tag{2.25}$$

We can finally cast (2.24) in Fourier space:

$$\delta\dot{\vec{\rho}}_q = -M_q \delta\vec{\rho}_q \tag{2.26}$$

with the *dynamical matrix* given by[1]:

$$M_q = q^2 \begin{pmatrix} D_1\rho_1\left(\frac{1}{\rho_1}+\partial_1\mu_1\right) & D_1\rho_1\,\partial_2\mu_1 & \cdots & \cdots & D_1\rho_1\,\partial_N\mu_1 \\ D_2\rho_2\,\partial_1\mu_2 & D_2\rho_2\left(\frac{1}{\rho_2}+\partial_2\mu_2\right) & D_2\rho_2\,\partial_3\mu_2 & \cdots & D_2\rho_2\,\partial_N\mu_2 \\ \vdots & & & & \vdots \\ D_N\rho_N\,\partial_1\mu_N & \cdots & \cdots & \cdots & D_N\rho_N\left(\frac{1}{\rho_N}+\partial_N\mu_N\right) \end{pmatrix} \tag{2.27}$$

We are now in the position of assessing the stability of the homogeneous profile with respect to a linear perturbation $\delta\vec{\rho}$. First, we note that the dynamical matrix depends on the Fourier mode q only through a proportionality factor, hence in our theory there is no mode selection at linear level.
Second, linearly unstable perturbations will correspond to eigenmodes of (2.26) whose associated eigenvalues have a negative real part. In particular, real eigenvalues correspond to *static patterns*, like the ones observed for mixing and demixing. On the contrary, an imaginary part in the eigenvalues will be responsible for *dynamic patterns*, like self-propelling bands.
The general N-species diagonalization problem is, however, complicated to tackle. One can therefore focus on the $N = 2$ case, where calculations are still manageable and where we can gain some quantitative insight on the mechanisms driving the linear instabilities.

Before proceeding, though, we need a piece of nomenclature. From (2.27), we observe that the elements of the dynamical matrix contain terms like:

$$\partial_i\mu_j = \frac{\partial}{\partial\rho_i}\log v_j \tag{2.28}$$

i.e. the responses of log-velocity of one species to density fluctuations of the other. Accordingly, we shall classify interactions by:

[1] To lighten notation we drop the 0 indices, assuming implicitly that all quantities are computed on the homogeneous profile.

Target:	Self: $\partial_i \mu_i$	Cross: $\partial_i \mu_j, \quad i \neq j$
Effect	Inhibitory: $\partial_i \mu_j < 0$	Activating: $\partial_i \mu_j > 0$

2.3.1 Dynamic patterns in binary mixtures: travelling bands

To begin with, let us re-write the expression of the dynamical matrix for $N = 2$:

$$M_q = q^2 \begin{pmatrix} D_{A,0} \cdot \rho_{A,0} \left(\dfrac{1}{\rho_{A,0}} + \partial_A \mu_A \right) & D_{A,0} \cdot \rho_{A,0}\, \partial_B \mu_A \\ \\ D_{B,0} \cdot \rho_{B,0}\, \partial_A \mu_B & D_{B,0} \cdot \rho_{B,0} \left(\dfrac{1}{\rho_{B,0}} + \partial_B \mu_B \right) \end{pmatrix} \tag{2.29}$$

Since we are looking for dynamic patterns, we should determine the conditions for which the eigenvalues of M are complex and have a negative real part. One can easily show that:

$$\lambda_{1,2} = \frac{\mathrm{Tr}(M) \pm \sqrt{\mathrm{Tr}(M)^2 - 4\mathrm{Det}(M)}}{2} \tag{2.30}$$

so the conditions for a dynamical instability are:

$$\begin{cases} \Delta(M) \equiv \mathrm{Tr}(M)^2 - 4\mathrm{Det}(M) < 0 \\ \mathrm{Tr}(M) < 0 \end{cases} \tag{2.31}$$

Let us start with the discriminant $\Delta(M)$. Carrying out the calculations, one obtains:

$$\left[D_{A;0} \cdot \rho_{A;0} \left(\frac{1}{\rho_{A;0}} + \partial_A \mu_A \right) - D_{B;0} \cdot \rho_{B;0} \left(\frac{1}{\rho_{B;0}} + \partial_B \mu_B \right) \right]^2 + 4 D_{A;0}\, D_{B;0}\, \rho_{A;0}\, \rho_{B;0}\, \partial_B \mu_A\, \partial_A \mu_B < 0 \tag{2.32}$$

We highlight that this condition can be achieved *only if* we have non-reciprocal interactions:

$$\partial_B \mu_A\, \partial_A \mu_B < 0 \tag{2.33}$$

This observation is in agreement with simulations, where travelling patterns could be achieved only if cross-interactions had opposite signs.
From the point of view of the dynamics, non-reciprocality is interpretable as a *run-and-chase* mechanism: one species - say A - activates the motility of the other, while B inhibits A's microscopic velocity. Since active particles tend to accumulate where they go slower, A-particles will try to stick to B-ones, while B-particles will tend to accumulate far from A-clusters. This run-and-chase mechanism can therefore lead to the onset of a travelling pattern.

In order for these waves not to be exponentially damped, the homogeneous profile must be unstable with respect to these perturbations, hence:

$$\mathrm{Re}(\lambda) < 0 \quad \Leftrightarrow \quad \mathrm{Tr}(M) < 0 \quad \Leftrightarrow$$
$$\boxed{D_{A;0} \cdot \rho_{A;0} \left(\frac{1}{\rho_{A;0}} + \partial_A \mu_A \right) + D_{B;0} \cdot \rho_{B;0} \left(\frac{1}{\rho_{B;0}} + \partial_B \mu_B \right) < 0} \tag{2.34}$$

This condition is satisfied either when both species are *self-inhibitory*, or when one is self-activating and the other is *strongly self-inhibitory*. From a physical standpoint, this can be interpreted as a mechanism apt to stabilizing dense clusters, preventing them to shrink and fade because of diffusion. Such clusters are in fact supposed to play the role of wavefronts in this travelling-band scenario: hence, this mechanism would be a way to stabilize the wavefronts.

However, simulations have shown that travelling bands can emerge even when the self-interaction is switched off. To see if this can be explained by non-linear effects, or else if our approximated dynamics fails, we test our simulations with different parameters. Shrinking the interaction radius, hence making interactions more local, we still observe travelling patterns, so we conclude that the issue is not in the locality approximation. Furthermore, increasing the homogeneous density and size of the system we still observe these dynamic bands, leading us to conclude that the issue is not in the mean-field approximation too.
Our idea is therefore that the linear truncation is not sufficient to explain travelling patterns, and that non-linearities play a non-negligible role in this scenario. Indeed, the importance of non-linearities is also known for the single-species case, where phase separation can be observed between the spinodal and binodal lines. Nonetheless, this path has not been investigated further for multi-component active systems, so it may be an interesting subject of future research.

2.3.2 Static patterns in binary mixtures: mixing, demixing

In order to have a static pattern emerging from a linear instability, M must admit two real eigenvalues, at least one of which should be negative. In order for the eignevalues to be real, the discriminant should be positive:

$$\Delta \equiv \mathrm{Tr}(M)^2 - 4\mathrm{Det}(M) \geq 0 \tag{2.35}$$

which eventually corresponds to:

$$\Delta \equiv \left[D_{A,0} \cdot \rho_{A,0} \left(\frac{1}{\rho_{A,0}} + \partial_A \mu_A \right) - D_{B,0} \cdot \rho_{B,0} \left(\frac{1}{\rho_{B,0}} + \partial_B \mu_B \right) \right]^2 + 4 D_{A,0} D_{B,0} \rho_{A,0} \rho_{B,0} \partial_B \mu_A \partial_A \mu_B \geq 0 \tag{2.36}$$

Assuming that this condition holds, then the homogeneous profile is *linearly stable* if and only if:

$$\lambda_{1,2} > 0 \quad \Leftrightarrow \quad \mathrm{Tr}(M) \pm \sqrt{\mathrm{Tr}(M)^2 - 4\mathrm{Det}(M)} > 0 \quad \Leftrightarrow \quad \begin{cases} \mathrm{Tr}(M) > 0 \\ \mathrm{Det}(M) > 0 \end{cases} \tag{2.37}$$

Explicitly:

$$\begin{cases} \mathrm{Tr}(M) > 0 & \Leftrightarrow \quad D_{A,0} \cdot \rho_{A,0} \left(\dfrac{1}{\rho_{A,0}} + \partial_A \mu_A \right) + D_{B,0} \cdot \rho_{B,0} \left(\dfrac{1}{\rho_{B,0}} + \partial_B \mu_B \right) > 0 \\ \mathrm{Det}(M) > 0 & \Leftrightarrow \quad D_{A,0} D_{B,0} \rho_{A,0} \rho_{B,0} \left[\left(\dfrac{1}{\rho_{A,0}} + \partial_A \mu_A \right) \left(\dfrac{1}{\rho_{B,0}} + \partial_B \mu_B \right) - \partial_B \mu_A \partial_A \mu_B \right] > 0 \end{cases} \tag{2.38}$$

If one of these conditions does not hold, then a linear perturbation will grow exponentially in time.

The above expressions (2.38) are still too complicated to draw some general conclusion that is somehow insightful. Nonehteless, a few interesting limiting cases can be analysed:

- As studied by Curatolo et al. in [16], in the absence of self-interactions $\partial_A \mu_A = \partial_B \mu_B = 0$, *mutual inhibition* or *mutual activation* can generate linear instabilities:

  $$\rho_{A,0} \rho_{B,0} \partial_A \mu_A \partial_B \mu_B > 1 \tag{2.39}$$

  This is the key ingredient that leads, at a macroscopic level, to mixing or demixing. In particular, let us focus on the unstable eigenvector:

  - If the two species are *mutually inhibitory* ($\partial_A \mu_B < 0$), then one can show that the two components of the eigenvector have the same sign. This means that the linear perturbation is such that peaks in the two species density are *colocalized*, and at the macroscopic level we have *mixing*.
  - On the contrary, if the two species are *mutually activating* ($\partial_A \mu_B > 0$), then the two components of the eigenvector have opposite signs. This means that peaks in the two species density are *delocalized*, and at the macroscopic level we have *demixing*.

- A possible extension to the previous case is when we introduce self interactions of equal sign (e.g. both self-inhibiting or both self-activating). In this case, we

have a linear instability if cross interactions are strongly reciprocal:

$$0 < \left(\frac{1}{\rho_{A,0}} + \partial_A \mu_A\right)\left(\frac{1}{\rho_{B,0}} + \partial_B \mu_B\right) < \partial_A \mu_A \, \partial_B \mu_B \tag{2.40}$$

In ohter words, if self-interactions are present but do not compete excessively with cross-ones, the demixing/mixing phenomena are fundamentally unaffected.

2.3.3 Mean-field phase diagram for binary mixtures

The results that we have obtained for the linear-stability analysis can be used to sketch a mean-field phase diagram. Starting from the specific functional form for the velocity used in simulations (2.1):

$$v_{i,X} = v_{0,X} \exp\left(-K_X \arctan\left(\frac{\rho_{i,X} - \rho_M}{L_f}\right) + J_X^Y \arctan\left(\frac{\rho_{i,Y} - \rho_M}{L_f}\right)\right)$$

we will be able to compare our analytical results with the numerics. To begin with, given the high number of parameters that are present in the microscopic model, we need to impose some constraints. As we have done in the simulations, we require:

- Constant tumbling rate $\alpha_A = \alpha_B = 1$
- Equal self-interaction $K_A = K_B = K$
- Equal low-density velocity $v_{0,A} = v_{0,B} = v_0$
- Equal homogeneous density $\rho_{0,A} = \rho_{0,B} = \rho_0$
- Density shift equal to the homogeneous density for both species: $\rho_M = \rho_0$
- Equal density scale $L_{f,A} = L_{f,B} = L_f$

Eventually, using (2.29) we can write the dynamical matrix M, and compute its eigenvalues and eigenvectors. It is convenient to introduce the following rescaled cross-interactions x, y and self-interaction z:

$$x = J_A^B \cdot \frac{\rho_0}{L_f} \qquad y = J_B^A \cdot \frac{\rho_0}{L_f} \qquad z = K \cdot \frac{\rho_0}{L_f} \tag{2.41}$$

so that the dynamical matrix eventually reads:

$$M = \frac{1}{2} v_0^2 \begin{pmatrix} 1-z & x \\ y & 1-z \end{pmatrix} \propto \begin{pmatrix} 1-z & x \\ y & 1-z \end{pmatrix} \tag{2.42}$$

The associated eigenvalues are easily computed:

$$\lambda_{\pm} = (1-z) \pm \sqrt{xy} \tag{2.43}$$

with the respective eigenvectors:

$$\mathbf{e}_+ = \begin{pmatrix} y \\ \sqrt{xy} \end{pmatrix} \qquad \mathbf{e}_- = \begin{pmatrix} y \\ -\sqrt{xy} \end{pmatrix} \tag{2.44}$$

Let us first consider *dynamic patterns*, corresponding to complex eigenvalues of the dynamical matrix (2.42). In this case, a necessary requirement is that cross-interactions have opposite signs: $xy < 0$. This is indeed in perfect agreement with our numerical observations (Figure 2.2, Figure 2.3). Nevertheless, our linear theory cannot capture any quantitative difference between floating clusters and proper bands (Figure 2.3, Figure 2.10).
Linear instability of the perturbation is guaranteed when the self-interaction is sufficiently strong, namely when $z > 1$. As remarked in subsection 2.3.1, however, nonlinear effects could account for the emergence of self-propelling bands even in the absence of self-interaction, like the ones observed in simulations.

Static patterns, on the other hand, correspond to real eigenvalues of the dynamical matrix (2.42). In this case, cross-interactions must have the same signs: $xy > 0$. Linear instability occurs when the smallest eigenvalue λ_- is negative. The corresponding eigenvector $\mathbf{e}_-$ can provide interesting information on the charachteristic of the perturbation:

- For $x, y > 0$, i.e. for mutually-activating strains, the two components of $\mathbf{e}_-$ have opposite signs. This corresponds to delocalization of the two strains, resulting in macroscopic *demixing* (Figure 2.5).
- On the contrary, when the two strains are mutually-inhibiting ($x, y < 0$), the two components of $\mathbf{e}_-$ have the same sign, corresponding to colocalization and hence macroscopic *mixing* (Figure 2.4).

In this scenario, what is the role of self-interactions? Given the expression of λ_- in eq. (2.43), increasing the value of z, static linear instabilities can emerge even for weaker cross-interactions (x, y). In other words, mixing or demixing can be induced by sufficiently strong self-interactions even if mutual activation / inhibition is weak. This result is in qualitative agreement with what has been observed in numerical

simulations (section 2.1, Figure 2.6).
Beyond qualitative descriptions, however, our linear theory is able to capture some quantitative properties of the static phase transitions with remarkable accuracy:

- In the absence of self-interactions z, when the cross-interactions x, y are equal we expect to enter the (de)mixed phase for a specific value $x^* = y^*$. Translating from rescaled to real interactions $J_A^B = J_B^A \equiv J$, the transition value J^* is in great agreement with numerical observations (Figure 2.9).

- If we set sufficiently weak cross-interactions $J_A^B = J_B^A = J$, then gradually increase the value of the self-interaction K, the transition from homogeneous to (de)mixed phase occurs at a value K^* that is perfectly compatible with simulations.

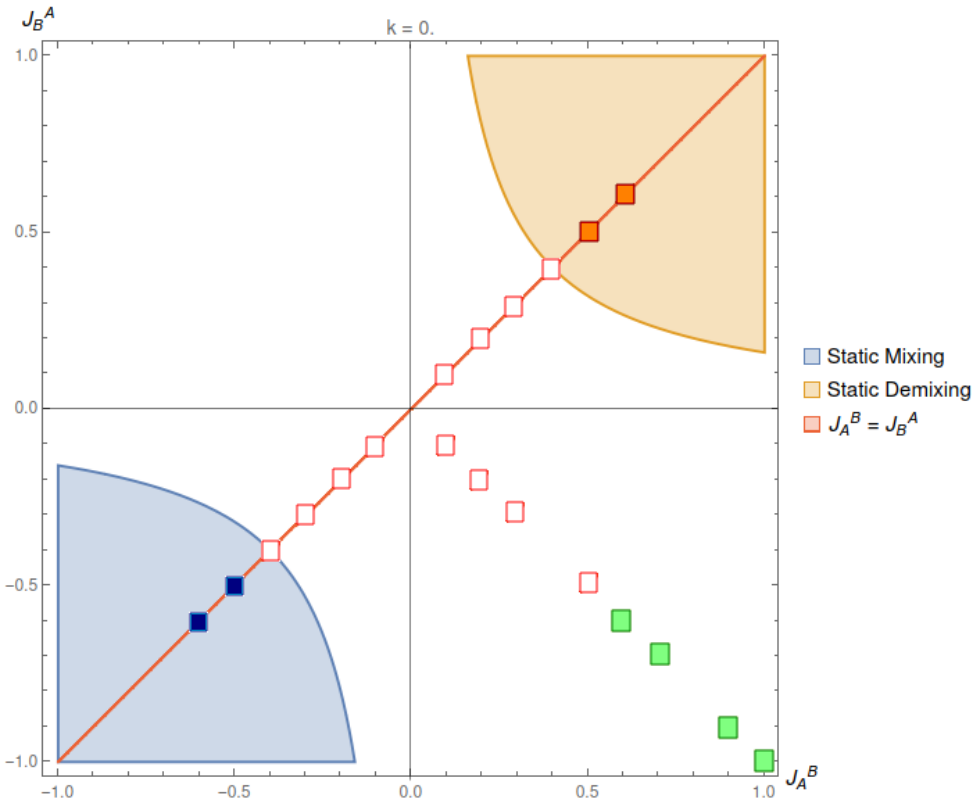

Figure 2.9: Mean-field phase diagram obtained from linear-stability analysis in the absence of self-interactions $K = 0$. The axes represent the self-interaction strengths J_A^B, J_B^A. Boxes correspond to the results of simulations. White-filled boxes correspond to simulations where the **homogeneous** phase is stable; blue boxes correspond to mixing, while orange boxes correspond to demixing; green boxes correspond to self-propelling bands. When $K = 0$, floating clusters are not observed.
As regards static patterns, the agreement between simulations and linear theory is remarkable, also from a quantitative point of view. Dynamic patterns in the absence of self-interaction, instead, cannot be captured by a linear theory.

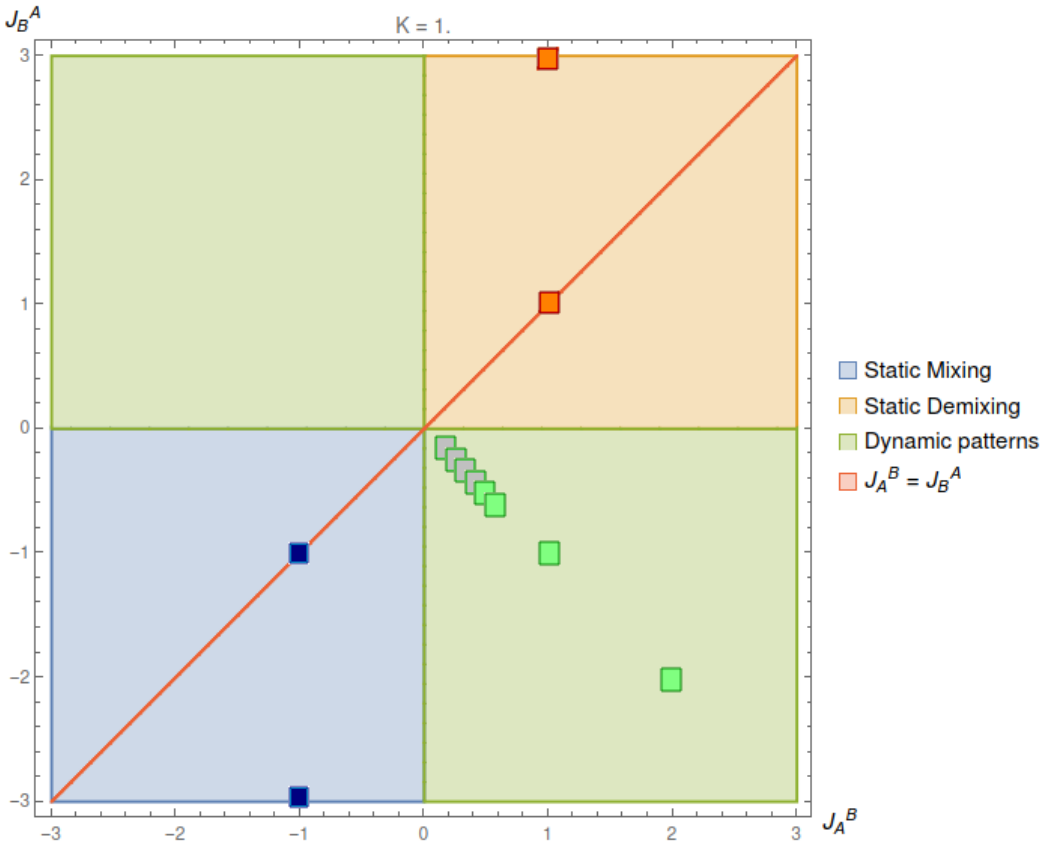

Figure 2.10: Mean-field phase diagram obtained from linear-stability analysis for self-interaction strength $K = 1$. The axes represent the self-interaction strengths J_A^B, J_B^A. Boxes correspond to the results of simulations. Blue boxes correspond to mixing, while orange boxes correspond to demixing; grey boxes correspond to dynamic floating clusters, while green-filled boxes correspond to self-propelling bands.
Both static and dynamic features of patterns are correctly predicted by the linear theory in this case; nonetheless, it cannot distinguish between floating clusters and proper bands.

In conclusion, we have seen how the linear stability theory can explain the essential properties of macroscopic patterns (dynamic vs. static, mixing vs. demixing). The full phenomenology of dynamic patterns, however, is still too complicated to be tackled by a linear theory, which cannot capture, for instance, the difference between floating clusters and bands. Most importantly, this level of description cannot account for the existence of dynamic structures in the absence of self-inhibition.
As far as static patterns are concerned, instead, the linear theory achieves remarkable results both from a qualitative and quantitative point of view. In fact, not only does it explain the emergence of colocalization / delocalization of the two strains, but it also provides good estimates of the critical parameters for our simulations.

Chapter 3

Being in or out-of equilibrium

In chapter 2, we have seen how active mixtures can exhibit a rich macroscopic dynamics when compared to passive systems or monodisperse active systems.
However, some of these patterns can be achieved by an equivalent passive system where particles interact via a properly-chosen potential U. In other words, in some cases it is possible to find a *mapping* between an active mixture and an equilibrium passive system such that the emerging macroscopic patterns are indistinguishable.
Of course, this is not true in general. Some macroscopic patterns emerging in active mixtures manifestly violate time-reversal symmetry, for example the self-propelling bands shown in Figure 2.2. In such cases, breaking of detailed balance by active particles is preserved throughout coarse-graining from microscopic to macroscopic, and hence no mapping to a passive system can be established.

In this chapter, we would like to explore this subject further, trying to establish which are the conditions on the microscopic dynamics that will ensure the existence of an equilibrium mapping at macroscopic scale. The main idea is to be look for a free energy functional for the macroscopic dynamics, and to relate its existence to specific forms of the microscopic velocity functional.

3.1 Chemical potential in the Cahn-Hilliard equation

The starting point of our analysis will be the set of macroscopic field equations (2.16) for N species. Indeed, in the absence of translational diffusion $D_t = 0$, it is convenient to re-write them as a set of *generalized Cahn-Hilliard* equations:

$$\dot{\rho}_i = \nabla[D_i \rho_i \nabla \mu_i + \sqrt{2D_i \rho_i}\Lambda] \qquad i = 1,\dots,N \tag{3.1}$$

where the chemical potential for species i is defined as:

$$\mu_i = \log v_i(\mathbf{r}, [\vec{\rho}]) + \log \rho_i(\mathbf{r}, [\vec{\rho}])) \tag{3.2}$$

It is known [22] that the Cahn-Hilliard equation (3.1) describes an equilibrium, i.e. time-reversible, field dynamics if and only if the chemical potential can be obtained as the functional derivative of a free energy functional $\mathscr{F}$.
In the chemical potential (3.2), it is straightforward to observe that $\log \rho_i$ can always be expressed as the derivative of a functional:

$$\log \rho_i(\mathbf{x}, [\vec{\rho}])) = -\frac{\delta \mathscr{S}}{\delta \rho_i(\mathbf{x})} \qquad \text{with } \mathscr{S}([\vec{\rho}]) = -\sum_{j=1}^{N} \int \mathrm{d}^2 x \, \rho_j(\mathbf{x})(\log \rho_j(\mathbf{x}) - 1) \tag{3.3}$$

Noting that ρ_i is a conserved field, $\forall i$ the term:

$$\int \mathrm{d}^2 x \, \rho_i(\mathbf{x}) = N_i$$

plays the role of an additive constant in $\mathscr{S}$, and is therefore irrelevant. Hence, if a free energy $\mathscr{F}$ exists, we can interpret:

$$\mathscr{S} = -\sum_{j=1}^{N} \int \mathrm{d}^2 x \, \rho_j(\mathbf{x}) \, \log \rho_j(\mathbf{x}) \tag{3.4}$$

as the entropic part of the free energy.
As a consequence, to determine the integrability conditions we can focus on the velocity term in (3.2), and seek an *excess free energy functional* $\mathscr{U}$:

$$\log v_i(\mathbf{x}, [\vec{\rho}])) = \frac{\delta \mathscr{U}}{\delta \rho_i(\mathbf{x})} \tag{3.5}$$

In case $\mathscr{U}$ exists, the total free energy $\mathscr{F}$ will be given by:

$$\mathscr{F} = \mathscr{U} - \mathscr{S} \tag{3.6}$$

which can be interpreted as a form of energy - entropy competition. The existence of $\mathscr{F}$ entails an equivalence at macroscopic level between the active system and a system of passive particles interacting in the $\mathscr{U}$ energy landscape [10].

3.2 Conditions for equilibrium

In the following, we will focus on different specific conditions for the velocity functionals $v_i(\mathbf{x},[\vec{\rho}])$. In each case, our goal will be to determine:

1. what is the type of velocity functionals ensuring an equilibrium mapping for the macroscopic dynamics;
2. what is the associated free energy.

3.2.1 Probing the existence of a free energy: functional Schwartz's criterion

The key tool to proceed towards our goal is a generalization of Schwartz's theorem for cross derivatives. In $\mathbb{R}^d$, it is known from standard calculus that a given vector field $\mathbf{E}$ can be written as the gradient of a scalar potential V if:

$$\partial_i E_j = \partial_j E_i \qquad \forall\, i,j \in \{1,\dots,d\} \tag{3.7}$$

This condition, namely Schwartz's theorem, is both necessary and sufficient if the domain on which $\mathbf{E}$ is defined is simply connected.

The above result can be extended [10] to functional vector fields as the chemical potential $\vec{\mu}$ introduced in (3.2). Let us define the distributions:

$$\mathscr{D}_{ij}(\mathbf{x},\mathbf{y}) \equiv \frac{\delta\mu_i(\mathbf{x})}{\delta\rho_j(\mathbf{y})} - \frac{\delta\mu_j(\mathbf{y})}{\delta\rho_i(\mathbf{x})} \qquad i,j \in \{1,\dots,N\} \tag{3.8}$$

Assuming that the space of functions $\vec{\rho}$ is simply connected, the existence of a free energy $\mathscr{F}$ is guaranteed if and only if $\mathscr{D}_{ij}$ is zero in the sense of distributions:

$$\boxed{\exists\,\mathscr{F}:\ \mu_i(\mathbf{x},[\vec{\rho}\,]) = \frac{\delta\mathscr{F}[\vec{\rho}\,]}{\delta\rho_i(\mathbf{x})} \quad \Leftrightarrow \quad \forall\,(i,j),\forall\psi,\phi: \quad \iint \mathscr{D}_{ij}(\mathbf{x},\mathbf{y})\psi(\mathbf{x})\phi(\mathbf{y}) = 0} \tag{3.9}$$

3.2.2 Local velocity functional

The first case that we can consider is the one of a local velocity functional, i.e. an expression:

$$v_i(\mathbf{x}, [\rho_1, \ldots, \rho_N]) = v_i(\rho_1(\mathbf{x}), \ldots, \rho_N(\mathbf{x})) \tag{3.10}$$

In words, the velocity of a particle of species i located at $\mathbf{x}$ is governed only by the density of all types of particles at that same point. The associated *excess* chemical potential μ_i is defined as:

$$\mu_i(\rho_1(\mathbf{x}), \ldots, \rho_N(\mathbf{x})) = \log v_i \tag{3.11}$$

The integrability Schwartz conditions (3.9) impose, for any two arbitrary functions φ, ψ:

$$\begin{aligned}
\forall\, i,j: \qquad & \int \left(\frac{\delta \mu_i(\mathbf{x})}{\delta \rho_j(\mathbf{y})} - \frac{\delta \mu_j(\mathbf{y})}{\delta \rho_i(\mathbf{x})} \right) \psi(\mathbf{x}) \varphi(\mathbf{y}) = 0 \\
\Rightarrow \quad & \int \left(\frac{\partial \mu_i(\mathbf{x})}{\partial \rho_j} - \frac{\partial \mu_j(\mathbf{y})}{\partial \rho_i} \right) \delta(\mathbf{x}-\mathbf{y}) \psi(\mathbf{x}) \varphi(\mathbf{y}) = 0 \\
\Rightarrow \quad & \int \left(\frac{\partial \mu_i(\mathbf{x})}{\partial \rho_j} - \frac{\partial \mu_j(\mathbf{x})}{\partial \rho_i} \right) \psi(\mathbf{x}) \varphi(\mathbf{x}) = 0
\end{aligned}$$

- If $i = j$, the above condition is always satisfied, since:

$$\frac{\partial \mu_i(\mathbf{x})}{\partial \rho_i} - \frac{\partial \mu_i(\mathbf{x})}{\partial \rho_i} = 0 \tag{3.12}$$

- If $i \neq j$, we obtain the condition:

$$\boxed{\frac{\partial \mu_i(\mathbf{x})}{\partial \rho_j} = \frac{\partial \mu_j(\mathbf{x})}{\partial \rho_i}} \tag{3.13}$$

  This is an example of *reciprocality* in QS: variations of ρ_i impinge on the log-velocity of species j in the same way as variations of ρ_j affect the log-velocity of species i. Equilibriumness, in this case, is therefore accompanied by an underlying symmetry of microscopic interactions.

At equilibrium, the associated *excess free energy* is:

$$\mathscr{U} = \int u(\rho_1(\mathbf{x}), \ldots, \rho_N(\mathbf{x}))\, \mathrm{d}^2 x \ : \qquad \mu_i(\mathbf{x}) = \frac{\partial u}{\partial \rho_i}(\mathbf{x}) \tag{3.14}$$

and the total free energy is therefore:

$$\boxed{\mathscr{F} = \int f(\rho_1(\mathbf{x}), \dots, \rho_N(\mathbf{x})) = \int u(\rho_1, \dots, \rho_N) - \sum_{i=1}^{N} \int -\rho_i \log \rho_i} \tag{3.15}$$

where, again, we recognise an energy-entropy interplay. Naturally, the resulting potential energy $\mathscr{U}$ is purely local, and can be obtained by integrating over space the potential energy density u.

3.2.3 Two-body-convolution velocity functional

Up to now, we have tackled the problem of the equilibrium mapping in a local framework. In this section, we shall see how non-localities in the velocity functional $v_i[\vec{\rho}]$ can affect the equilibrium mapping in active mixtures, adding further constraints with respect to (3.13).

Let us assume that v_i can be expressed as a function of effective densities $\tilde{\rho}_i$, i.e.:

$$v_i(\mathbf{x}, [\rho_1, \dots, \rho_N]) \equiv v_i(\tilde{\rho}_i^1, \dots, \tilde{\rho}_i^N), \tag{3.16}$$

where the effective densities $\tilde{\rho}_i^j$ are defined as:

$$\tilde{\rho}_i^j(\mathbf{x}) \equiv (K_i^j * \rho_j)(\mathbf{x}) = \int \mathrm{d}^2 y \, K_i^j(\mathbf{x}, \mathbf{y}) \, \rho_j(\mathbf{y}) \tag{3.17}$$

K_i^j are convolution kernels that mediate the interaction between the particle under study (species i) and a neighbour of species j. K_i^j can be seen as representing an intermediate chemical field c_i^j produced by bacterium i and sensed by bacterium j, see eq. (1.5). Note that in principle K_i^j and K_j^i can be different, implying a *non-reciprocal interaction* between the two species. For example, one particle of type i can increase its velocity in presence of a j particle, while the j particle inhibits its velocity when close to an i particle.
We assume the following properties for the kernels:

- *Translational invariance*

$$K_i^j(\mathbf{x}, \mathbf{y}) = K_i^j(\mathbf{x} - \mathbf{y}) \tag{3.18}$$

- *Reflection symmetry*

$$K_i^j(\mathbf{x}) = K_j^i(-\mathbf{x}) \qquad \forall \mathbf{x}, \quad \forall (i,j) \tag{3.19}$$

To give an example, one can take K_i^j to be a bell-shaped function whose support is a disc of radius d[1]:

$$K_i^j(\mathbf{r}) = \frac{1}{Z}\,\theta(d-r)\,\exp\left[-\frac{d^2}{d^2-r^2}\right] \tag{3.20}$$

where Z is a normalization constant such that $\int \mathrm{d}^2 r\, K_i^j = 1$.

We introduce the following notation for the derivative with respect to the effective density[2]:

$$\partial_i^j \equiv \frac{\partial}{\partial \tilde{\rho}_i^j} \tag{3.21}$$

so that: $\partial_A^A = \partial_{\tilde{\rho}_A^A}$, $\partial_A^B = \partial_{\tilde{\rho}_A^B}$ ... and so on. The Schwartz condition (3.9), states that equilibrium is achieved iff:

$$\begin{cases} \partial_i^i \log v_i(\mathbf{x}) = \alpha_i^i \ \in \mathbb{R} & \forall \mathbf{x}, \forall i \in \{1,\dots,N\} \\ K_j^i(\mathbf{x}-\mathbf{y})\,\partial_j^i \log v_j(\mathbf{x}) = K_i^j(\mathbf{x}-\mathbf{y})\,\partial_i^j \log v_i(\mathbf{y}) & \forall \mathbf{x},\ \mathbf{y}, \forall i \neq j \end{cases} \tag{3.22}$$

It can be proved that[3], in order to fulfil these conditions for all $\mathbf{x},\mathbf{y}$, the interactions between a particle of species i and one of species j should be *reciprocal* at equilibrium, meaning that $K_j^i = K_i^j$. We can therefore drop upper and lower indices, introducing the symmetric kernels $K_{ij} \equiv K_i^j = K_j^i$. This property represents a form of *action-reaction* statement for the QS-interacting strains, and we shall call it *reciprocal symmetry* or *reciprocality*.
Eventually, the only admissible form for the velocity functional is:

$$\boxed{v_i(\mathbf{x}) = v_{i;0} \cdot \exp\left\{ \sum_{j=1}^{N} \alpha_{ij} \int \mathrm{d}^2 y\, K_{ij}(\mathbf{x}-\mathbf{y})\rho_j(\mathbf{y}) \right\} \quad \text{with } \alpha_{ij} = \alpha_{ji},\ K_{ij} = K_{ji}} \tag{3.23}$$

where the coefficients α_i^j are constrained to be symmetrical.

[1] We remark here that this type of convolutional kernel is used also in simulations (Appendix A).

[2] The double-index notation is in fact necessary because, in principle, the effective density of a given species X is different when observed by a particle of type A or type B, i.e. in general $K_i^j \neq K_j^i$.

[3] See Appendix D for full detail of calculations.

The most general form of a free energy $\mathscr{F}$ is then:

$$\boxed{\mathscr{F} = \mathscr{U} - \mathscr{S} = \sum_{i,j} \frac{1}{2}\alpha_{ij} \iint K_{ij}(\mathbf{x}-\mathbf{y})\rho_i(\mathbf{x})\rho_j(\mathbf{y}) + \sum_{i=1}^{N} \int \rho_i \log \rho_i} \tag{3.24}$$

In conclusion we have shown that, under reciprocal symmetry at microscopic level, these active systems can be mapped into a passive system of particles interacting via a 2-body effective potential $\mathscr{U}$. This potential contains all terms of intra-species (K_{ii}) and inter-species interactions (K_{ij}).

Chapter 4

Conclusions and future research

4.1 Conclusions

In this work, we studied the dynamics of an N-component mixture of RTPs interacting via QS, with special focus on the emergent macroscopic phenomenology.

Numerical simulations of the microscopic dynamics were employed to study the emergent large-scale phases in a binary mixture. One of the most important results is the observation of self-propelling bands, which had not been obtained so far from microscopic simulations. Our results tally with the ones by R. Golenstanian et al. in [17], where they show, starting from hydrodynamic simulations, that non-reciprocal cross-interactions are necessary in order to generate dynamic structures.
Besides, we examined some new aspects in the phenomenology of static patterns. First of all, we showed how a sufficiently strong self-inhibition can lead to mixing or demixing even if cross-interactions are weak. Second, we saw how a macroscopic separation of timescales can occur if one cross-interaction is much stronger than the other.

In order to provide physical grounds to the numerical observations, we coarse-grained the microscopic theory and derived the macroscopic evolution of the density fields. The coarse-graining procedure was analogous to the one presented in [16], with the difference that we considered RTPs with instantaneous tumbles.
Making use of mean-field approximation and linear stability analysis, we studied how small perturbations can affect the stability of a homogeneous profile. In this way we could provide some quantitative predictions on the emergent phases as a function of the microscopic interactions.
At this stage, we were able to compare our analytical predictions with the numerical

observations. Our results are in qualitative agreement with the numerics, shedding light on the mechanisms that lead to the emergence of patterns. In the case of static patterns, we could also provide quantitative predictions with a remarkable level of accuracy.
Nonetheless, a linear treatment is not fully satisfactory: in the context of dynamic patterns, it cannot account for the emergence of bands when the self-interaction is switched off, nor can it describe the transition from floating clusters to bands.

Finally, in chapter 3 we studied when active mixtures can be mapped into a macroscopically equivalent passive system. To do so, we re-expressed the field dynamics in the form of a Cahn-Hilliard equation, introducing a vector chemical potential $\vec{\mu}$. If $\vec{\mu}$ is an integrable field, then a free energy functional $\mathscr{F}$ exists for the dynamics. The problem could then be reformulated as finding the integrability conditions for $\vec{\mu}$. The mathematical tool to tackle this question was Schwartz's theorem for functionals. Eventually, we considered two specific cases for the functional form of the microscopic velocity: a local dependence $v(\vec{\rho})$ and a dependence on effective densities obtained by convolutions $K * \rho$. In both cases, we proved that the necessary ingredient to ensure equilibrium is reciprocality of microscopic cross-interactions. In the local case, this is also a sufficient condition. In the second case, further restrictions appeared, and the resulting potential energy $\mathscr{U}$ must be a quadratic form of the densities ρ_i.

4.2 What is next?

The internship work presented here is preliminary to my future Ph.D. project on *Self-organization and morphogenesis of active mixtures*, which will be carried out under the supervision of Julien Tailleur at the Laboratoire Matière et Systèmes Complexes (MSC) of the Université de Paris. The project will also benefit from an external collaboration with Mehran Kardar, a leading expert on statistical field theory at MIT.

Our research is aimed at elucidating the phenomenology of increasingly complex active mixtures. In biology, such knowledge would be extremely important to clarify morphogenetic mechanisms, like embryogenesis. Ideally, once we have a deep understanding on how to translate microscopic interactions into macroscopic patterns, we could think of engineering synthetic systems that are capable of self-assembling into a desired shape. Such technology could be important in biomedical engineering, for example in the design of artificial tissues.

Practically speaking, what are the next steps to take in this research?
First, even though several analytical results have been obtained in the general N-component framework, the phenomenological part of our work was mainly centered on binary mixtures. The next step will therefore be to extend simulations to generic N-component mixtures, to see whether new interesting phases can emerge.
In order to gain further understanding on the N-component case, one possible idea could be to introduce random interactions between strains, resorting to random matrix theory. In this regards, we could benefit from collaborations with other members of Laboratoire MSC, namely Frédéric van Wijland and Ada Altieri, experts on glassy systems.

Second, in our discussion we have only considered the role of interactions to generate different macroscopic phases, keeping the homogeneous densities fixed at the same value $\rho_{0,A} = \rho_{0,B}$. An alternative view on the problem could be to fix the interaction strengths and vary the composition of the mixture.

Furthermore, in subsection 2.3.1 we highlighted how a linear treatment of the field theory cannot tell the full story on macroscopic phenomenology, even for binary mixtures. In particular, some phenomena associated with dynamic patterns could not be accounted for, like the transition from floating clusters to bands and the emergence of bands even in the absence of self-interactions. It is therefore necessary to go beyond a linear treatment, and study how non-linearities affect the emergence of macroscopic patterns.

Finally, beyond phenomenological aspects, the statistical physics of the macroscopic dynamics would deserve further studies. It could be interesting to focus on correlations and critical properties of the field theory, employing tools such as the Janssen - De Dominicis formalism and renormalization group. To this end, the collaboration with Mehran Kardar at MIT will be of paramount importance.

To draw our conclusions, this work was meant to present the first steps in the study of active mixtures, trying to bridge the gap from microscopic to macroscopic dynamics. Already at the level of binary mixtures, non-trivial, fascinating phenomena can be observed. The hope for the future is to enrich the class of emergent phases, while gaining a deeper understanding of the relation between microscopic parameters and large-scale behaviours. Even if the path is still long, the perspectives on the applications of these studies are very exciting, and will hopefully guide our way in the future of the project.

References

[1] Marjolein N. van der Linden, Lachlan C. Alexander, Dirk G. A. L. Aarts, and Olivier Dauchot. Interrupted motility induced phase separation in aligning active colloids. *Phys. Rev. Lett.*, 123:098001, Aug 2019.

[2] Antoine Bricard, Jean-Baptiste Caussin, Nicolas Desreumaux, Olivier Dauchot, and Denis Bartolo. Emergence of macroscopic directed motion in populations of motile colloids. *Nature*, 503(7474):95–98, Nov 2013.

[3] Shashi Thutupalli, Delphine Geyer, Rajesh Singh, Ronojoy Adhikari, and Howard A Stone. Flow-induced phase separation of active particles is controlled by boundary conditions. *Proceedings of the National Academy of Sciences of the United States of America*, 115(21):5403—5408, May 2018.

[4] Xiaolu Wang, Martin In, Christophe Blanc, Alois Würger, Maurizio Nobili, and Antonio Stocco. Janus colloids actively rotating on the surface of water. *Langmuir*, 33(48):13766–13773, 2017. PMID: 29116797.

[5] Delphine Geyer, David Martin, Julien Tailleur, and Denis Bartolo. Freezing a flock: Motility-induced phase separation in polar active liquids. *Phys. Rev. X*, 9:031043, Sep 2019.

[6] Julius B Kirkegaard and Raymond E Goldstein. The role of tumbling frequency and persistence in optimal run-and-tumble chemotaxis. *IMA Journal of Applied Mathematics*, 83(4):700–719, 07 2018.

[7] Howard Berg and Richard Berry. E. coli in motion. *Physics Today*, 58:64–65, 02 2005.

[8] Marco Polin, Idan Tuval, Knut Drescher, J. P. Gollub, and Raymond E. Goldstein. Chlamydomonas swims with two "gears" in a eukaryotic version of run-and-tumble locomotion. *Science*, 325(5939):487–490, 2009.

[9] R. Sunyer, V. Conte, J. Escribano, A. Elosegui-Artola, A. Labernadie, L. Valon, D. Navajas, J. M. García-Aznar, J. J. Muñoz, P. Roca-Cusachs, and X. Trepat. Collective cell durotaxis emerges from long-range intercellular force transmission. *Science*, 353(6304):1157–1161, 09 2016.

[10] J. O'Byrne and J. Tailleur. Lamellar to micellar phases and beyond: When tactic active systems admit free energy functionals. *Physical Review Letters*, 125(20), Nov 2020.

[11] Michael E. Cates and Julien Tailleur. Motility-induced phase separation. *Annual Review of Condensed Matter Physics*, 6(1):219–244, Mar 2015.

[12] Hugues Chaté and Benoît Mahault. Dry, aligning, dilute, active matter: A synthetic and self-contained overview, 2019.

[13] Julien Tailleur and M. Cates. Sedimentation, trapping, and rectification of dilute bacteria. *EPL (Europhysics Letters)*, 86:60002, 03 2009.

[14] Alexandre Solon, M. Cates, and Julien Tailleur. Active brownian particles and run-and-tumble particles: a comparative study. *The European Physical Journal Special Topics*, 224, 04 2015.

[15] J. Tailleur and M. E. Cates. Statistical mechanics of interacting run-and-tumble bacteria. *Physical Review Letters*, 100(21), May 2008.

[16] A. I. Curatolo, N. Zhou, Y. Zhao, C. Liu, A. Daerr, J. Tailleur, and J. Huang. Cooperative pattern formation in multi-component bacterial systems through reciprocal motility regulation. *Nature Physics*, 16(11):1152–1157, August 2020.

[17] Suropriya Saha, Jaime Agudo-Canalejo, and Ramin Golestanian. Scalar active mixtures: The nonreciprocal cahn-hilliard model. *Phys. Rev. X*, 10:041009, Oct 2020.

[18] Curatolo. *Collective behaviours in living systems: from bacteria to molecular motors.* PhD thesis, Université Paris-Diderot, 2017.

[19] Alexandre P Solon, Joakim Stenhammar, Michael E Cates, Yariv Kafri, and Julien Tailleur. Generalized thermodynamics of motility-induced phase separation: phase equilibria, laplace pressure, and change of ensembles. *New Journal of Physics*, 20(7):075001, Jul 2018.

[20] Chenli Liu, Xiongfei Fu, Lizhong Liu, Xiaojing Ren, Carlos K.L. Chau, Sihong Li, Lu Xiang, Hualing Zeng, Guanhua Chen, Lei-Han Tang, Peter Lenz, Xiaodong Cui, Wei Huang, Terence Hwa, and Jian-Dong Huang. Sequential establishment of stripe patterns in an expanding cell population. *Science*, 334(6053):238–241, 2011.

[21] M. E. Cates and J. Tailleur. When are active brownian particles and run-and-tumble particles equivalent? consequences for motility-induced phase separation. *EPL (Europhysics Letters)*, 101(2):20010, Jan 2013.

[22] P. M. Chaikin and T. C. Lubensky. *Principles of Condensed Matter Physics*. Cambridge University Press, 1995.

Appendix A

Simulations

In this appendix, we provide the details on the microscopic simulations of active mixtures. During my internship, I have developed a `C` code from scratch that simulates the coupled Langevin dynamics of N particles belonging to K different classes. In the binary case, 2 species of RTPs interact via quorum-sensing. The simulation volume is divided in cells of side d, and each particle can interact only with others in the same cell or in the first-neighbouring cells, within a finite radius d.
At each time interval $(t, t+dt)$:

- For each particle i, the local effective density of species X is computed, weighing the relative distance between particles through a smooth bell-shaped kernel:

$$\tilde{\rho}_{i;X} = \sum_{\substack{j:\,\mathrm{Label}(j)=X \\ |\mathbf{r}_i-\mathbf{r}_j|<d}} \frac{1}{Z}\exp\left(-\frac{d^2}{d^2-|\mathbf{r}_i-\mathbf{r}_j|^2}\right) \tag{A.1}$$

  with normalization $Z = 2\pi d^2 \int_0^1 dx \exp\left(-\frac{1}{1-x^2}\right)$

- Each particle's speed is updated according to the local density of particles of the same and of the other species (QS-interaction). For a particle i belonging to species X:

$$v_{i,X} = v_0 \exp\left(-K \arctan\left(\frac{\tilde{\rho}_{i,X}-\rho_M}{L}\right) + J_X^Y \arctan\left(\frac{\tilde{\rho}_{i,Y}-\rho_M}{L}\right)\right) \tag{A.2}$$

- We set a sequence of tumbling times $\{t_i\}$ in the interval $(t, t+dt)$. More precisely, the i-th tumbling event occurs at t_i:

$$t_i = t_{i-1} + \tau_i \qquad \text{with } t_0 = t \tag{A.3}$$

  where τ_i is drawn from an exponential distribution $p(\tau_i) = \alpha \exp(-\alpha\tau_i)$, α being the tumbling rate. Random numbers τ_i are drawn until we find a value $\tau_n : t_{n+1} > t+dt$. If that happens, we stop our sequence at t_n.

- Each particle moves in a straight line with speed v until the first tumbling event, then it changes its orientation drawing the final angle θ' from a uniform distribution. Subsequently, it continues to move in the θ' direction with same speed v until the next tumbling event. The run-and-tumble motion is iterated until the end of the time interval.

A.1 Single-species test

To validate the code, I tested it in the limit case of single species, with the aim of reconstructing the phase diagram for QS-MIPS as in A. Solon et al. [19]. In order to compare with the results of the paper, we use a functional form of the velocity:

$$v_i(\tilde{\rho}) = v_0 + \frac{v_1 - v_0}{2}\left[1 + \tanh\left(2\frac{\tilde{\rho}}{\rho_m} - 2\right)\right] \tag{A.4}$$

which is the one used in [19]. At high local densities, the velocity will tend to v_1, while v_0 corresponds to the low-density speed. When $v_1 < v_0$, crowding will slow particles down.
Simulations are performed in a square of size 50×50, with tumbling rate $\alpha = 1$, interaction range $d = 1$, $\rho_m = 200$. High-density velocity is set to $v_1 = 5$, while v_0 is varied in the simulations.
When phase coexistence is observed, we wait for the system to thermalize and sample the local density in each box. Averaging over time, a density histogram is produced, with two peaks corresponding to the liquid and gas phase densities (Figure A.1). Eventually, the binodal curves are reconstructed. As we can observe from Figure A.2, our curve is in great agreement with the one in [19].

A.1.1 Binary mixture: details of simulations

Having tested the correct functioning of the code on the single-species case, we can carry out simulations on binary mixtures. In our simulations, we vary the strength and sign of interactions $\{K_X, J_X^Y\}$, in order to observe different phases. Besides, we focus on the case $K_A = K_B = K$, so as to reduce the space of parameters to be explored. This choice is mostly motivated by the fact that, in the initial exploration of numerical results, no relevant phenomena seemed to emerge by playing with different self-interactions.
For both species we take $v_0 = 2$, and fix the initial homogeneous density at $\rho_{0,A} = \rho_{0,B} = 100$. The density offset ρ_M is the same for both species, and is set to 40. Finally, the density scale L_f is set to 40 for both A and B. The tumbling rate α is assumed to be constant equal to 1 for both species, and translational noise is switched off $D_t = 0$.

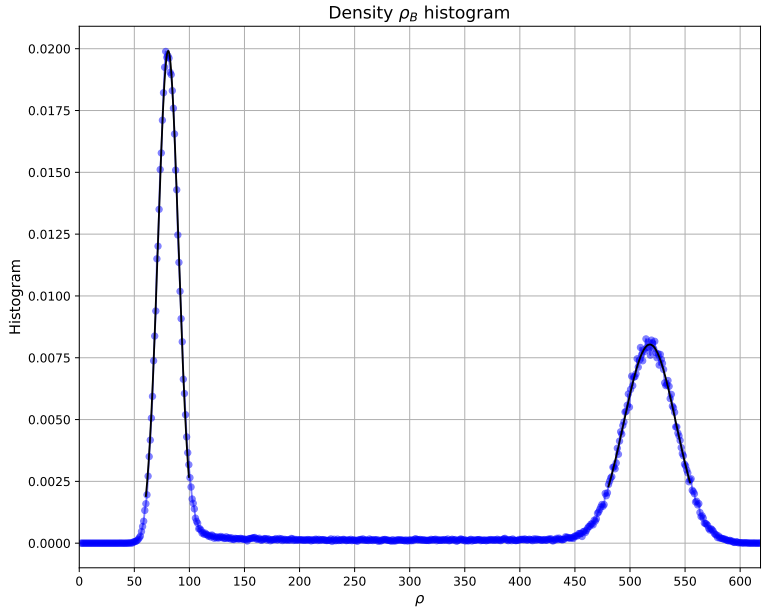

Figure A.1: Example of averaged density histogram for a single-species simulation with $v_1 = 5$, $v_0 = 35$. Histogram peaks are fitted with gaussian functions to retrieve the liquid and gas phase density.

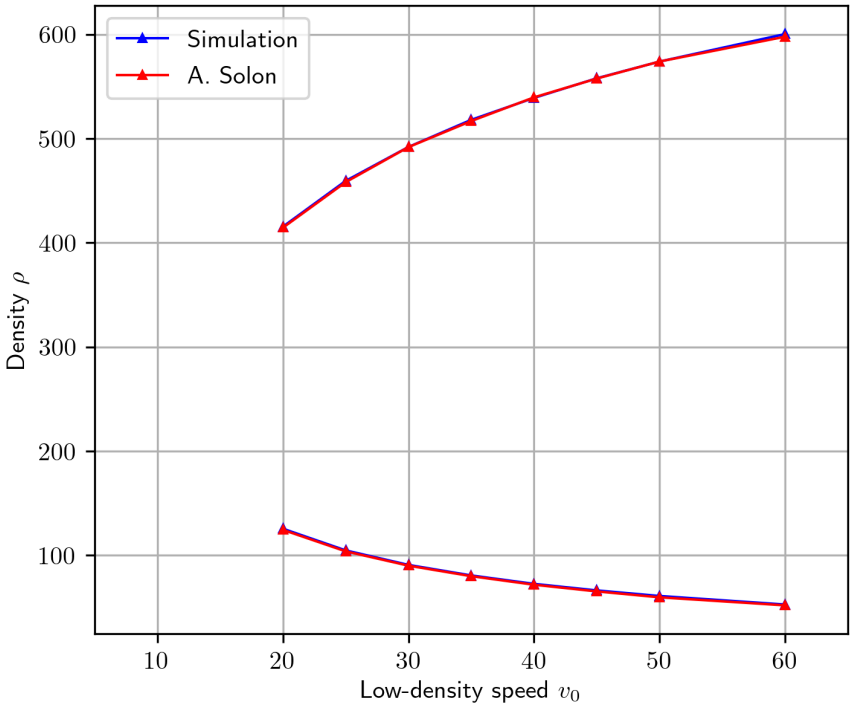

Figure A.2: Binodal curves obtained from simulations: comparison between our simulations (blue) and A. Solon's data (red) from [19]. Simulations are performed in a square of size 50×50, with $v_1 = 5$, tumbling rate $\alpha = 1$, interaction range $d = 1$, $\rho_m = 200$.

Appendix B

Coarse-graining

B.1 Dean procedure from mesoscopic Langevin to macroscopic field theory

In this appendix, we provide a full derivation for the N-species macroscopic field dynamics (2.16) starting from the mesoscopic Langevin equations (2.13):

$$\dot{\mathbf{r}}_i = \mathbf{V}_X(\mathbf{r}_i,[\vec{\rho}]) + \nabla_{\mathbf{r}_i} D_X(\mathbf{r}_i,[\vec{\rho}]) + \sqrt{2D_X(\mathbf{r}_i,[\vec{\rho}])}\,\xi(t) \tag{B.1}$$

$$\xi \;:\; \text{Gaussian white noise with } \langle \xi_i(t)\xi_j(t')\rangle = \delta_{i,j}\delta(t-t') \tag{B.2}$$

First of all, we define the density of particles of species X as:

$$\rho_X(\mathbf{r},t) = \sum_{i:\ \mathrm{Label}(i)=X} \delta(\mathbf{r}-\mathbf{r}_i(t)) \tag{B.3}$$

Then, we introduce an arbitrary function g_X of the position of X-particles, such that:

$$g_X(\{\mathbf{r}_i\}) = \sum_{i:\ \mathrm{Label}(i)=X} g(\mathbf{r}_i) \tag{B.4}$$

The idea to derive the evolution of ρ_X is the following: first, we write the evolution of g_X in two different ways, with dependence on ρ_X and $\dot{\rho}_X$. Eventually, if we equate these two expressions, exploiting the arbitrariness of g we will conclude on the dynamics of ρ_X.

- *First expression*. Using the definition of ρ_X:

$$\begin{aligned} g_X(\{\mathbf{r}_i\}) &= \sum_{i:\,\text{Label}(i)=X} g(\mathbf{r}_i) && \text{(B.5)} \\ &= \sum_{i:\,\text{Label}(i)=X} \int \mathrm{d}r\, g(\mathbf{r})\, \delta(\mathbf{r}-\mathbf{r}_i(t)) && \text{(B.6)} \\ &= \int \mathrm{d}r\, g(\mathbf{r}) \sum_{i:\,\text{Label}(i)=X} \delta(\mathbf{r}-\mathbf{r}_i(t)) = \int \mathrm{d}r\, g(\mathbf{r})\, \rho_X(\mathbf{r},t) && \text{(B.7)} \end{aligned}$$

  Hence, the time derivative of g_X can be expressed as:

$$\frac{dg_X}{dt} = \int \mathrm{d}r\, g(\mathbf{r})\, \partial_t \rho_X(\mathbf{r},t) \tag{B.8}$$

- *Second expression*. Another way to express the time derivative of g_X is by means of the Ito chain-rule. Starting from the definition of g_X:

$$\frac{dg_X}{dt} = \sum_{i:\,\text{Label}(i)=X} \frac{d}{dt} g(\mathbf{r}_i) \tag{B.9}$$

  Applying the Ito chain-rule to $g(\mathbf{r}_i)$:

$$\begin{aligned} \frac{d}{dt} g(\mathbf{r}_i) &= \dot{\mathbf{r}}_i \cdot \nabla_{\mathbf{r}_i} g(\mathbf{r}_i) + D \nabla^2_{\mathbf{r}_i} g(\mathbf{r}_i) \\ &= \left(\mathbf{V}_X(\mathbf{r}_i,[\vec{\rho}]) + \nabla_{\mathbf{r}_i} D_X(\mathbf{r}_i,[\vec{\rho}]) + \sqrt{2D_X(\mathbf{r}_i,[\vec{\rho}])}\xi_i(t) \right) \cdot \nabla_{\mathbf{r}_i} g(\mathbf{r}_i) \\ &\quad + D_X(\mathbf{r}_i,[\vec{\rho}]) \cdot \nabla^2_{\mathbf{r}_i} g(\mathbf{r}_i) \end{aligned}$$

  We can re-write this expression making use of δ functions:

$$\begin{aligned} \frac{d}{dt} g(\mathbf{r}_i) = &\int \mathrm{d}r\, \delta(\mathbf{r}-\mathbf{r}_i) \left(\mathbf{V}_X(\mathbf{r},[\vec{\rho}]) + \nabla_{\mathbf{r}_i} D_X(\mathbf{r},[\vec{\rho}]) \right) \cdot \nabla_{\mathbf{r}} g(\mathbf{r}) \\ &+ \int \mathrm{d}r\, \delta(\mathbf{r}-\mathbf{r}_i)\, D_X(\mathbf{r},[\vec{\rho}]) \cdot \nabla^2_{\mathbf{r}} g(\mathbf{r}) \\ &+ \int \mathrm{d}r\, \delta(\mathbf{r}-\mathbf{r}_i)\, \xi_i(t) \sqrt{2D_X(\mathbf{r},[\vec{\rho}])} \cdot \nabla_{\mathbf{r}} g \end{aligned} \tag{B.10}$$

  Now, in the first two integrals, all dependences on the particle's position have been entirely shifted on the $\delta(\mathbf{r}_i-\mathbf{r})$ functions. This will come in very useful in the following. Note that, instead, the stochastic term still yields a dependence on i both on the δ-function and on ξ_i.

We can finally write the evolution of the entire g_X, plugging (B.10) in (B.9):

$$\frac{dg_X}{dt} = \int \mathrm{d}r \sum_{i:\ \mathrm{Label}(i)=X} \delta(\mathbf{r}_i - \mathbf{r}) \left\{ \left(\mathbf{V}_X(\mathbf{r},[\vec{\rho}]) + \nabla_{\mathbf{r}} D_X(\mathbf{r},[\vec{\rho}]) \right) \cdot \nabla_{\mathbf{r}} g(\mathbf{r}) + D_X(\mathbf{r},[\vec{\rho}]) \cdot \nabla^2_{\mathbf{r}} g(\mathbf{r}) \right\}$$
$$+ \int \mathrm{d}r \sum_{i:\ \mathrm{Label}(i)=X} \delta(\mathbf{r}_i - \mathbf{r})\, \xi_i(t) \sqrt{2D_X(\mathbf{r},[\vec{\rho}])} \cdot \nabla_{\mathbf{r}} g(\mathbf{r}) \tag{B.11}$$

In the first integral, the only terms depending on $\mathbf{r}_i$ are the $\delta(\mathbf{r}-\mathbf{r}_i)$, so we can identify and isolate ρ_X inside the integral:

$$\frac{dg_X}{dt} = \int \mathrm{d}r\, \rho_X(\mathbf{r}) \left\{ \left(\mathbf{V}_X(\mathbf{r},[\vec{\rho}]) + \nabla_{\mathbf{r}} D_X(\mathbf{r},[\vec{\rho}]) \right) \cdot \nabla_{\mathbf{r}} g(\mathbf{r}) + D_X(\mathbf{r},[\vec{\rho}]) \cdot \nabla^2_{\mathbf{r}} g(\mathbf{r}) \right\}$$
$$+ \int \mathrm{d}r \sum_{i:\ \mathrm{Label}(i)=X} \delta(\mathbf{r} - \mathbf{r}_i)\, \xi_i(t) \sqrt{2D_X(\mathbf{r},[\vec{\rho}])} \cdot \nabla_{\mathbf{r}} g(\mathbf{r}) \tag{B.12}$$

The latter integral contains a sum of gaussian random variables, hence it can be re-expressed as a *gaussian random field* $\Lambda(\mathbf{r},t)$:

$$\int \mathrm{d}r \sum_{i:\ \mathrm{Label}(i)=X} \delta(\mathbf{r} - \mathbf{r}_i)\, \xi_i(t) \sqrt{2D_X(\mathbf{r},[\vec{\rho}])} \cdot \nabla_{\mathbf{r}} g = \int \mathrm{d}r\, \nabla_{\mathbf{r}} g(\mathbf{r}) \sqrt{2D_X(\mathbf{r},[\vec{\rho}])\rho_X}\ \Lambda(\mathbf{r},t) \tag{B.13}$$

where:

$$\langle \Lambda_\alpha(\mathbf{r},t) \Lambda_\beta(\mathbf{r}',t') \rangle = \delta_{\alpha,\beta}\, \delta(\mathbf{r}-\mathbf{r}')\delta(t-t') \tag{B.14}$$

Finally, we are left to deal with the first line of (B.12). Integrating by parts, we eventually end up with:

$$-\int \mathrm{d}r\, g(\mathbf{r})\, \nabla_{\mathbf{r}} \cdot \left\{ \left(\mathbf{V}_X(\mathbf{r},[\vec{\rho}]) + \nabla_{\mathbf{r}} D_X(\mathbf{r},[\vec{\rho}]) \right) \rho_X(\mathbf{r}) - \nabla_{\mathbf{r}} \left(D_X(\mathbf{r},[\vec{\rho}]) \rho_X(\mathbf{r}) \right) \right\} \tag{B.15}$$

which can be further simplified by expanding the term $\nabla_{\mathbf{r}}(D_X \rho_X)$:

$$-\int \mathrm{d}r\, g(\mathbf{r})\, \nabla_{\mathbf{r}} \cdot \left\{ \mathbf{V}_X(\mathbf{r},[\vec{\rho}]) \rho_X - D_X(\mathbf{r},[\vec{\rho}]) \nabla_{\mathbf{r}} \rho_X(\mathbf{r}) \right\} \tag{B.16}$$

Finally, putting together the results obtained from eqs. (B.13) and (B.16) we conclude:

$$\frac{dg_X}{dt} = -\int \mathrm{d}r\, g(\mathbf{r})\, \nabla_{\mathbf{r}} \cdot \left\{ \mathbf{V}_X(\mathbf{r},[\vec{\rho}]) \rho_X - D_X(\mathbf{r},[\vec{\rho}]) \nabla_{\mathbf{r}} \rho_X + \sqrt{2D_X(\mathbf{r},[\vec{\rho}])\rho_X}\ \Lambda(\mathbf{r},t) \right\} \tag{B.17}$$

We can eventually compare the two expressions (B.8), (B.17) for the time derivative of g_X to conclude. Indeed, exploiting the fact that g is arbitrary, the two integrands

must be the same, hence:

$$\partial_t \rho_X = -\nabla_{\mathbf{r}} \cdot \left\{ \mathbf{V}_X(\mathbf{r}, [\vec{\rho}]) \rho_X - D_X(\mathbf{r}, [\vec{\rho}]) \nabla_{\mathbf{r}} \rho_X + \sqrt{2 D_X(\mathbf{r}, [\vec{\rho}]) \rho_X}\ \Lambda(\mathbf{r}, t) \right\} \tag{B.18}$$

which is the macroscopic field equation that we were looking for.

Appendix C

Linear stability analysis of the field theory

C.1 Linearization procedure of the mean-field theory

In this appendix, we present the full calculation for the linearization of the mean-field N-species theory (2.21). We recall the mean-field equations:

$$\dot{\rho}_i(\mathbf{r}) = -\nabla\cdot[\mathbf{V}_i(\mathbf{r},[\vec{\rho}])\rho_i(\mathbf{r}) - D_i(\mathbf{r},[\vec{\rho}])\nabla\rho_i(\mathbf{r})] \tag{C.1}$$

$$D_i = \frac{1}{2}\frac{v_i^2(\mathbf{r},[\vec{\rho}])}{\alpha_i(\mathbf{r},[\vec{\rho}])} \qquad i\in\{1,\dots,N\} \tag{C.2}$$

$$\mathbf{V}_i = -\frac{1}{2}\frac{v_i\nabla v_i(\mathbf{r},[\vec{\rho}])}{\alpha_i(\mathbf{r},[\vec{\rho}])} \tag{C.3}$$

Let $\rho_i = \rho_{i,0} + \delta\rho_i$, where all $\rho_{i,0}$ are homogeneous fields and $\delta\rho_i$ are small perturbations.
Since $\rho_{i,0}$ is a homogeneous field, we incidentally observe that:

$$\nabla\rho_i = \nabla\rho_{i,0} + \nabla\delta\rho_i = \nabla\delta\rho_i \tag{C.4}$$

Assuming locality of the microscopic velocity v_i and tumbling rate α_i, we can expand (C.1) to linear order in $\delta\vec{\rho}$. Let us start with the term $D_i\nabla\rho_i$:

$$D_i = \frac{1}{2}\frac{v_i^2(\vec{\rho}_0+\delta\vec{\rho})}{\alpha(\vec{\rho}_0+\delta\vec{\rho})} = \frac{1}{2}\frac{v_i^2(\vec{\rho}_0)}{\alpha(\vec{\rho}_0)} + \mathscr{O}(\delta\vec{\rho}) \tag{C.5}$$

$$\Rightarrow D_i\nabla\rho_i = D_i\nabla\delta\rho_i = \left(\frac{1}{2}\frac{v_i^2(\vec{\rho}_0)}{\alpha(\vec{\rho}_0)} + \mathscr{O}(\delta\vec{\rho})\right)\nabla\delta\rho_i \tag{C.6}$$

$$= \frac{1}{2}\frac{v_i^2(\vec{\rho}_0)}{\alpha(\vec{\rho}_0)}\nabla\delta\rho_i + \mathscr{O}(\delta\rho^2) \equiv \tag{C.7}$$

$$= D_{i,0}\nabla\delta\rho_i + \mathscr{O}(\delta\rho^2) \tag{C.8}$$

Next, we can expand the drift term $\mathbf{V}_i\rho_i$:

$$\mathbf{V_i} = -\frac{1}{2}\frac{v_i(\vec{\rho}_0+\delta\vec{\rho})\ \nabla v_i(\vec{\rho}_0+\delta\vec{\rho})}{\alpha(\vec{\rho}_0+\delta\vec{\rho})} = \tag{C.9}$$

$$= -\frac{1}{2}\frac{v_i(\vec{\rho}_0)\ \nabla\left[v_i(\vec{\rho}_0) + \sum_{j=1}^N \partial_j v_i\cdot\delta\rho_j\right]}{\alpha(\vec{\rho}_0)} + \mathscr{O}(\delta\rho^2) \tag{C.10}$$

We note that the derivatives $\partial_j v_i$ are evaluated at $\vec{\rho}_0$, hence they are constants with respect to space and can be brought out of the ∇ operator:

$$\mathbf{V_i} = -\frac{1}{2}\frac{v_i(\vec{\rho}_0)}{\alpha(\vec{\rho}_0)}\cdot\left(\sum_{j=1}^N \partial_j v_i\ \nabla\delta\rho_j\right) + \mathscr{O}(\delta\rho^2) \tag{C.11}$$

$$\Rightarrow \mathbf{V_i}\rho_i = -\rho_{i,0}\cdot\frac{1}{2}\frac{v_i(\vec{\rho}_0)}{\alpha(\vec{\rho}_0)}\cdot\left(\sum_{j=1}^N \partial_j v_i\ \nabla\delta\rho_j\right) + \mathscr{O}(\delta\rho^2) \tag{C.12}$$

Recalling the expression of $D_{i,0}$, we can re-elaborate (C.12):

$$\mathbf{V_i}\rho_i = -\rho_{i,0}\cdot\frac{D_{i,0}}{v_{i,0}}\cdot\left(\sum_{j=1}^N \partial_j v_i\ \nabla\delta\rho_j\right) + \mathscr{O}(\delta\rho^2) \tag{C.13}$$

$$= -\rho_{i,0}\cdot D_{i,0}\cdot\left(\sum_{j=1}^N \frac{1}{v_{i,0}}\partial_j v_i\ \nabla\delta\rho_j\right) + \mathscr{O}(\delta\rho^2) \tag{C.14}$$

$$= -D_{i,0}\rho_{i,0}\cdot\left(\sum_{j=1}^N \partial_j \log v_i\ \nabla\delta\rho_j\right) + \mathscr{O}(\delta\rho^2) \tag{C.15}$$

We can now plug the linearized expressions (C.8), (C.15) inside the mean-field equations:

$$\delta\dot{\rho}_i = D_{i,0}\,\rho_{i,0}\left[\sum_{j=1}^N \partial_j \log v_{i,0}\,\nabla^2\delta\rho_j + \frac{1}{\rho_{i,0}}\nabla^2\delta\rho_i\right] + \mathscr{O}(\delta\rho^2) \tag{C.16}$$

Eventually, we define the *excess local chemical potentials* on the homogeneous profile $\mu_i \equiv \log v_{i,0}$, so that the linear expansion of field equation becomes:

$$\delta\dot{\rho}_i = D_{i,0}\,\rho_{i,0}\left[\sum_{j=1}^N \partial_j \mu_i\,\nabla^2\delta\rho_j + \frac{1}{\rho_{i,0}}\nabla^2\delta\rho_i\right] + \mathscr{O}(\delta\rho^2) \tag{C.17}$$

Introducing the Fourier transform of the density perturbation:

$$\delta\vec{\rho}_{\mathbf{q}} = \int d^2x\, e^{-i\mathbf{q}\cdot\mathbf{x}}\ \delta\vec{\rho}(\mathbf{x}) \tag{C.18}$$

We can finally cast (C.17) in Fourier space:

$$\delta\dot{\vec{\rho}}_q = -M_q \delta\vec{\rho}_q \tag{C.19}$$

with the *dynamical matrix*[1]:

$$M_q = q^2 \begin{pmatrix} D_1\,\rho_1\left(\dfrac{1}{\rho_1}+\partial_1\mu_1\right) & D_1\,\rho_1\,\partial_2\mu_1 & \cdots & \cdots & D_1\,\rho_1\,\partial_N\mu_1 \\ D_2\,\rho_2\,\partial_1\mu_2 & D_2\,\rho_2\left(\dfrac{1}{\rho_2}+\partial_2\mu_2\right) & D_2\,\rho_2\,\partial_3\mu_2 & \cdots & D_2\,\rho_2\,\partial_N\mu_2 \\ \vdots & & & & \vdots \\ D_N\,\rho_N\,\partial_1\mu_N & \cdots & \cdots & \cdots & D_N\,\rho_N\left(\dfrac{1}{\rho_N}+\partial_N\mu_N\right) \end{pmatrix} \tag{C.20}$$

[1] To lighten notation we drop the 0 indices, assuming implicitly that all quantities are computed on the homogeneous profile.

Appendix D

Mapping to Equilibrium

D.1 Two-body convolution velocity functional

In order to impose the Schwartz conditions (3.9), we need to compute the functional derivatives of the excess chemical potential:

$$\frac{\delta \mu_i(\mathbf{x})}{\delta \rho_j(\mathbf{y})} = \frac{\delta}{\delta \rho_j(\mathbf{y})} \log v_i(\tilde{\rho}_i^1(\mathbf{x}), \ldots, \tilde{\rho}_i^N(\mathbf{x})) \tag{D.1}$$

$$= \partial_i^j \log v_i(\mathbf{x}) \cdot \frac{\delta \tilde{\rho}_i^j(\mathbf{x})}{\delta \rho_j(\mathbf{y})} \tag{D.2}$$

$$= \partial_i^j \log v_i(\mathbf{x}) \cdot K_i^j(\mathbf{x}-\mathbf{y}) \tag{D.3}$$

We now need to impose the equality of cross-derivatives according to (3.9). In order to do so, we shall consider separately the case $i = j$ and $i \neq j$.

- $i = j$:

$$\frac{\delta \mu_i(\mathbf{x})}{\delta \rho_i(\mathbf{y})} = \frac{\delta \mu_i(\mathbf{y})}{\delta \rho_i(\mathbf{x})} \quad \Longleftrightarrow \quad \partial_i^i \log v_i(\mathbf{x}) \cdot K_i^i(\mathbf{x}-\mathbf{y}) = \partial_i^i \log v_i(\mathbf{y}) \cdot K_i^i(\mathbf{y}-\mathbf{x}) \quad \forall\, \mathbf{x}, \mathbf{y} \tag{D.4}$$

  Exploiting the $\mathbf{x} \to -\mathbf{x}$ symmetry of the kernel, the K_i^i terms simplify:

$$\partial_i^i \log v_i(\mathbf{x}) = \partial_i^i \log v_i(\mathbf{y}) \qquad \forall\, \mathbf{x}, \mathbf{y} \tag{D.5}$$

  Since the two sides of (D.5) depend on different variables, we conclude that:

$$\partial_i^i \log v_i(\mathbf{x}) = \alpha_i^i \ \in \mathbb{R} \tag{D.6}$$

Integrating this equation with respect to $\tilde{\rho}_i^i$:

$$\boxed{v_i(\mathbf{x}) = \exp\{ \quad \alpha_i^i \cdot \tilde{\rho}_i^{\,i} + \psi_i^i(\tilde{\rho}_i^{\,1}, \ldots, \tilde{\rho}_i^{\,i-1}, \tilde{\rho}_i^{\,i+1}, \ldots, \tilde{\rho}_i^{\,N}) \quad \}} \tag{D.7}$$

where ψ_i^i is an (yet) unknown function of all the remaining effective densities around a particle of species i.

- $i \neq j$:

$$\frac{\delta \mu_i(\mathbf{x})}{\delta \rho_j(\mathbf{y})} = \frac{\delta \mu_j(\mathbf{y})}{\delta \rho_i(\mathbf{x})} \qquad \Longleftrightarrow \qquad \partial_i^j \log v_i(\mathbf{x}) \cdot K_i^j(\mathbf{x}-\mathbf{y}) = \partial_j^i \log v_j(\mathbf{y}) \cdot K_j^i(\mathbf{y}-\mathbf{x}) \quad \forall\, \mathbf{x}, \mathbf{y} \tag{D.8}$$

We rewrite the above equation in the form:

$$\frac{\partial_i^j \log v_i(\mathbf{x})}{\partial_j^i \log v_j(\mathbf{y})} = \frac{K_j^i(\mathbf{y}-\mathbf{x})}{K_i^j(\mathbf{x}-\mathbf{y})} \tag{D.9}$$

In order to understand which functions v_i, K_i^j, K_j^i can solve (D.9), we define:

$$f(\mathbf{x}) \equiv \partial_i^j \log v_i(\mathbf{x}) \tag{D.10}$$

$$g(\mathbf{y}) \equiv \partial_j^i \log v_j(\mathbf{y}) \tag{D.11}$$

$$h(\mathbf{z}) \equiv \frac{K_j^i(-\mathbf{z})}{K_i^j(\mathbf{z})} \qquad \text{with} \quad h(\mathbf{z}) = h(-\mathbf{z}) \tag{D.12}$$

Having introduced these auxiliary functions, eq. (D.9) can be re-expressed as:

$$\frac{f(\mathbf{x})}{g(\mathbf{y})} = h(\mathbf{x}-\mathbf{y}) \qquad \text{with} \quad h(\mathbf{x}-\mathbf{y}) = h(\mathbf{y}-\mathbf{x}) \tag{D.13}$$

We claim the following:

> **Lemma**.
> *Equation* (D.13) *is solved only by functions of the form:*
>
> $$f(\mathbf{x}) = \gamma \qquad g(\mathbf{y}) = 1 \qquad h(\mathbf{z}) = \gamma \qquad\qquad \gamma \in \mathbb{R} \tag{D.14}$$
>
> *or by any scalar multiple of these:* $\alpha \cdot f, \alpha \cdot g, \alpha \cdot h$.

We now present the proof of this statement, with the remark that its details are not relevant to the rest of the discussion and can be skipped.

Proof of the lemma.

- To begin with, we note that, if f, g, h are three functions solving (D.13), also $\alpha \cdot f, \alpha \cdot g, \alpha \cdot h$ are solutions.
  We can therefore choose arbitrarily the normalization of the solutions, and in particular we take $g(\mathbf{0}) = 1$.

- Consider $\mathbf{y} = \mathbf{0}$ in (D.13). Then:

$$\frac{f(\mathbf{x})}{g(\mathbf{0})} = h(\mathbf{x}) \qquad \Rightarrow \qquad h(\mathbf{x}) = f(\mathbf{x}) \tag{D.15}$$

- Take $\mathbf{x} = \mathbf{0}$ in (D.13). Then, exploiting the result we have just obtained:

$$\frac{f(\mathbf{0})}{g(\mathbf{y})} = h(-\mathbf{y}) = h(\mathbf{y}) = f(\mathbf{y}) \qquad \Rightarrow \qquad g(\mathbf{y}) = \frac{f(\mathbf{0})}{f(\mathbf{y})} \tag{D.16}$$

- Finally, plugging back expressions (D.15), (D.16) into (D.13), we have:

$$\frac{f(\mathbf{x})}{f(\mathbf{y})} f(\mathbf{0}) = f(\mathbf{x} - \mathbf{y}) \tag{D.17}$$

  This is indeed the functional equation defining the exponential function, thus:

$$f(\mathbf{x}) = \gamma \cdot e^{\lambda \cdot \mathbf{x}} \qquad \gamma \in \mathbb{R},\ \lambda \in \mathbb{R}^d \tag{D.18}$$

$$\Rightarrow h(\mathbf{x}) = f(\mathbf{x}) = \gamma \cdot e^{\lambda \cdot \mathbf{x}} \tag{D.19}$$

$$g(\mathbf{x}) = e^{\lambda \cdot \mathbf{x}} \tag{D.20}$$

  Finally, requiring that $h(\mathbf{x}) = h(-\mathbf{x})$, we conclude $\lambda = 0$ and thus:

$$f(\mathbf{x}) = \gamma \qquad g(\mathbf{y}) = 1 \qquad h(\mathbf{z}) = \gamma \qquad \gamma \in \mathbb{R} \tag{D.21}$$

  proving our thesis. $\square$

Making use of the *Lemma* and the definition of functions f, g, h:

$$\begin{cases} \partial_i^j \log v_i(\mathbf{x}) = \alpha_i^j \in \mathbb{R} \\ \partial_j^i \log v_j(\mathbf{y}) = 1 \\ \dfrac{K_j^i(\mathbf{z})}{K_i^j(\mathbf{z})} = \alpha_i^j \in \mathbb{R} \end{cases} \tag{D.22}$$

Integrating the first two equations of the system over $\tilde{\rho}_i^j$ and $\tilde{\rho}_j^i$ respectively, we obtain:

$$v_i(\mathbf{x}) = \exp\{ \alpha_i^j \int K_i^j \rho_j + \psi_i^j(\tilde{\rho}_i^1, \ldots, \tilde{\rho}_i^{j-1}, \tilde{\rho}_i^{j+1}, \ldots, \tilde{\rho}_i^N) \} \tag{D.23}$$

$$v_j(\mathbf{x}) = \exp\{ \int K_i^j \rho_i + \psi_j^i(\tilde{\rho}_j^1, \ldots, \tilde{\rho}_j^{i-1}, \tilde{\rho}_j^{i+1}, \ldots, \tilde{\rho}_j^N) \} \tag{D.24}$$

where ψ_i^j, ψ_j^i are unknown functions of the remaining effective densities. Finally, exploiting the last equation in (D.22), we can relate the two kernels:

$$K_j^i = \alpha_i^j K_i^j \tag{D.25}$$

and in conclusion:

$$v_i(\mathbf{x}) = \exp\{ \alpha_i^j \int K_i^j \rho_j + \psi_i^j(\tilde{\rho}_i^1, \ldots, \tilde{\rho}_i^{j-1}, \tilde{\rho}_i^{j+1}, \ldots, \tilde{\rho}_i^N) \} \tag{D.26}$$

$$v_j(\mathbf{x}) = \exp\{ \alpha_i^j \int K_i^j \rho_i + \psi_j^i(\tilde{\rho}_j^1, \ldots, \tilde{\rho}_j^{i-1}, \tilde{\rho}_j^{i+1}, \ldots, \tilde{\rho}_j^N) \} \tag{D.27}$$

Under the light of this reciprocity symmetry of equilibrium kernels, we can eventually drop the $\begin{smallmatrix} j \\ i \end{smallmatrix}$ index notation and write:

$$\boxed{v_i(\mathbf{x}) = \exp\{ \alpha_{ij} \int K_{ij} \rho_j + \psi_i^j(\tilde{\rho}_i^1, \ldots, \tilde{\rho}_i^{j-1}, \tilde{\rho}_i^{j+1}, \ldots, \tilde{\rho}_i^N) \}} \tag{D.28}$$

$$\boxed{v_j(\mathbf{x}) = \exp\{ \alpha_{ij} \int K_{ij} \rho_i + \psi_j^i(\tilde{\rho}_j^1, \ldots, \tilde{\rho}_j^{i-1}, \tilde{\rho}_j^{i+1}, \ldots, \tilde{\rho}_j^N) \}} \tag{D.29}$$

We are now in the position of determining the general form of the *equilibrium mi-*

croscopic velocity: making use of the results of equations (D.7), (D.28), (D.29) we conclude that the only admissible expression is:

$$\boxed{v_i(\mathbf{x}) = v_{i;0} \cdot \exp\left\{ \sum_{j=1}^{N} \alpha_{ij} \int \mathrm{d}^2 y \, K_{ij}(\mathbf{x}-\mathbf{y}) \rho_j(\mathbf{y}) \right\} \quad \text{with } \alpha_{ij} = \alpha_{ji},\ K_{ij} = K_{ji}} \tag{D.30}$$

Taking the logarithm of v_i, i.e. the excess chemical potential, and integrating it with respect to the density fields, we finally obtain the free energy functional (3.24):

$$\boxed{\mathscr{F} = \sum_{i,j} \frac{1}{2} \alpha_{ij} \iint K_{ij}(\mathbf{x}-\mathbf{y}) \rho_i(\mathbf{x}) \rho_j(\mathbf{y}) - \sum_{i=1}^{N} \int -\rho_i \log \rho_i} \tag{D.31}$$